Geology and geochemistry of gold mineralization at the Namicupo prospect, Mozambique Belt, northeastern Mozambique

Nopeia, Manuel

Imai, Akira

Takahashi, Ryohei

Yonezu, Kotaro

他

https://hdl.handle.net/2324/7330088

出版情報：Journal of Geochemical Exploration. 249, pp.107220-, 2023-06. Elsevier
バージョン：

Journal of Geochemical Exploration 249 (2023) 107220

Contents lists available at ScienceDirect

Journal of Geochemical Exploration

journal homepage: www.elsevier.com/locate/gexplo

Geology and geochemistry of gold mineralization at the Namicupo prospect, Mozambique Belt, northeastern Mozambique

Manuel Nopeia [a,b,*], Akira Imai [a], Ryohei Takahashi [c], Kotaro Yonezu [a], Pearlyn Manalo [c], Thomas Tindell [a], Hinako Sato [c], Daúd Jamal [d], Andrea Agangi [c]

[a] *Department of Earth Resources Engineering, Kyushu University, Fukuoka 819-0395, Japan*
[b] *Center for Regional Revitalization in Research and Education, Akita University, Akita 010-8502, Japan*
[c] *Department of Earth Resource Science, Akita University, Akita 010-8502, Japan*
[d] *Department of Geology, Eduardo Mondlane University, Maputo 257, Mozambique*

ARTICLE INFO

Keywords:
Namicupo gold prospect
Orogenic-type gold
Supergene enrichment
Mozambique Belt
Mozambique

ABSTRACT

Auriferous quartz veins in the Namicupo gold prospect occur parallel to the foliation of metasedimentary host rocks of the Xixano Complex in northeastern Mozambique. The geochemistry and ore-forming mechanism of the Namicupo prospect have never been scientifically investigated. This study discusses the ore mineralogy, fluid inclusion, and stable isotope (S-O) characteristics of the prospect. The mineralization in the Namicupo prospect is divided into two stages. The Stage I, primary mineralization, is represented by electrum with Ag contents of 15–26 at.%, associated with pyrite and chalcopyrite. The Stage II is supergene mineralization, characterized by electrum with Ag contents of 39–46 at.%, intergrown with goethite, barite, and minium, which replaced primary sulfides. Quartz from the mineralized veins hosts three types of primary fluid inclusions coexisting in the same fluid inclusion assemblage. Type A inclusions are three-phase aqueous-carbonic inclusions (aqueous liquid, CO_2 liquid and vapor), with final homogenization temperature and salinity varying from 140 to 241 °C, and 1.0 to 7.8 wt% NaCl eq., respectively. Type B inclusions occur either as mono-phase (vapor or liquid) or two-phase (vapor and liquid) CO_2-rich, N_2-H_2O-bearing inclusions, with homogenization temperature varying from +12.9 to +29.3 °C. The Type C inclusions are two-phase (liquid and vapor) aqueous inclusions, which homogenize to liquid phase at temperatures between 209 and 337 °C. The salinity of the Type C inclusions varies from 4.0 to 10.8 wt% NaCl eq. The sulfur isotopic ratios ($\delta^{34}S_{CDT}$) of sulfides associated with Stage I mineralization and the oxygen isotopic ratios ($\delta^{18}O_{SMOW}$) of water calculated from those of quartz from the quartz veins vary from −3.5 to +0.9 ‰ and −1.0 to +2.5 ‰, respectively.

The primary mineralization at the prospect is classified as an orogenic-type gold mineralization, formed by aqueous-carbonic metamorphic fluids. The precipitation of primary gold mineralization in the Namicupo prospect resulted dominantly from fluid immiscibility. The considerable amount of S up to 0.1 wt% and the high Ag contents of electrum intergrown with goethite, minium and barite suggest that the supergene mineralization in the Stage II was caused by oxidation of primary gold-bearing sulfides and Au-rich electrum under moderately acidic and oxidizing conditions, which resulted in Au and Ag liberation, likely by thiosulfate. Dissolution of primary mineralization and supergene gold enrichment in the Namicupo prospect appear to have occurred largely in situ, with little evidence of distant mobilization.

1. Introduction

Mozambique has a high potential for precious and base metals (Lächelt, 2004; Nopeia et al., 2021; Cossa et al., 2023), although mineral exploration in the country is relatively undeveloped. In fact, currently, artisanal and small-scale mining accounts for most of the gold produced in Mozambique (Hilson et al., 2021; Nopeia et al., 2022). The ongoing artisanal and small-scale mining is unveiling important geological features associated with primary gold mineralization, which should be studied from the viewpoint of economic geology.

Northeastern Mozambique lies within the Mozambique Belt, a segment of the East African Orogen, also referred to as the East African-

---

* Corresponding author at: Center for Regional Revitalization in Research and Education, Akita University, Akita 010-8502, Japan.
E-mail address: manuelnopeia@yahoo.com (M. Nopeia).

https://doi.org/10.1016/j.gexplo.2023.107220
Received 3 July 2022; Received in revised form 23 March 2023; Accepted 4 April 2023

Antarctic Orogen (Fig. 1a–b; Meert, 2003; Fritz et al., 2013). Although the geology and tectonic evolution of the Mozambique Belt in northeastern Mozambique have been widely investigated (Pinna et al., 1993; Jamal, 2005; Norconsult Consortium, 2007; Viola et al., 2008; Boyd et al., 2010; Grantham et al., 2013; Macey et al., 2013), the mineral endowment of the region is less studied. Norconsult Consortium (2007) and Korkiakoski (2008), based on a geochemical investigation of stream sediments, proposed potential areas for further exploration of precious and base metals, which could lead to significant discoveries in northeastern Mozambique. Currently, limited peer-reviewed studies on gold mineralization in the region include those of Bjerkgard et al. (2009), which constrained the nature and age of gold mineralization in the Niassa Gold Belt to the west (Fig. 1a), and Nopeia et al. (2021) that reported the geological and geochemical characteristics of the Nanlia and Makorongo prospects, located about 50 km east of the Namicupo prospect in Cabo Delgado Province (Fig. 2). In this study, we investigated the Namicupo prospect which is a part of the so-called Namuno-Napiço gold area (Lächelt, 2004). The amount of gold produced annually by artisanal miners in the Namicupo prospect was estimated to be about 10 kg (Nopeia et al., 2022).

This study is part of a pioneer project that aims to exhaustively describe the mode of occurrence, the geochemical characteristics, and age of gold mineralization in the Mozambique Belt of northeastern Mozambique to establish a comprehensive metallogenic model of gold mineralization, thus fostering further exploration in the region. This paper aims to describe the geological and geochemical characteristics of gold mineralization at the Namicupo prospect, which have never previously been scientifically reported. A detailed petrography, mineral chemistry, fluid inclusion and stable isotope studies were combined to constrain the mode of occurrence and the formation mechanisms of gold mineralization in the Namicupo prospect.

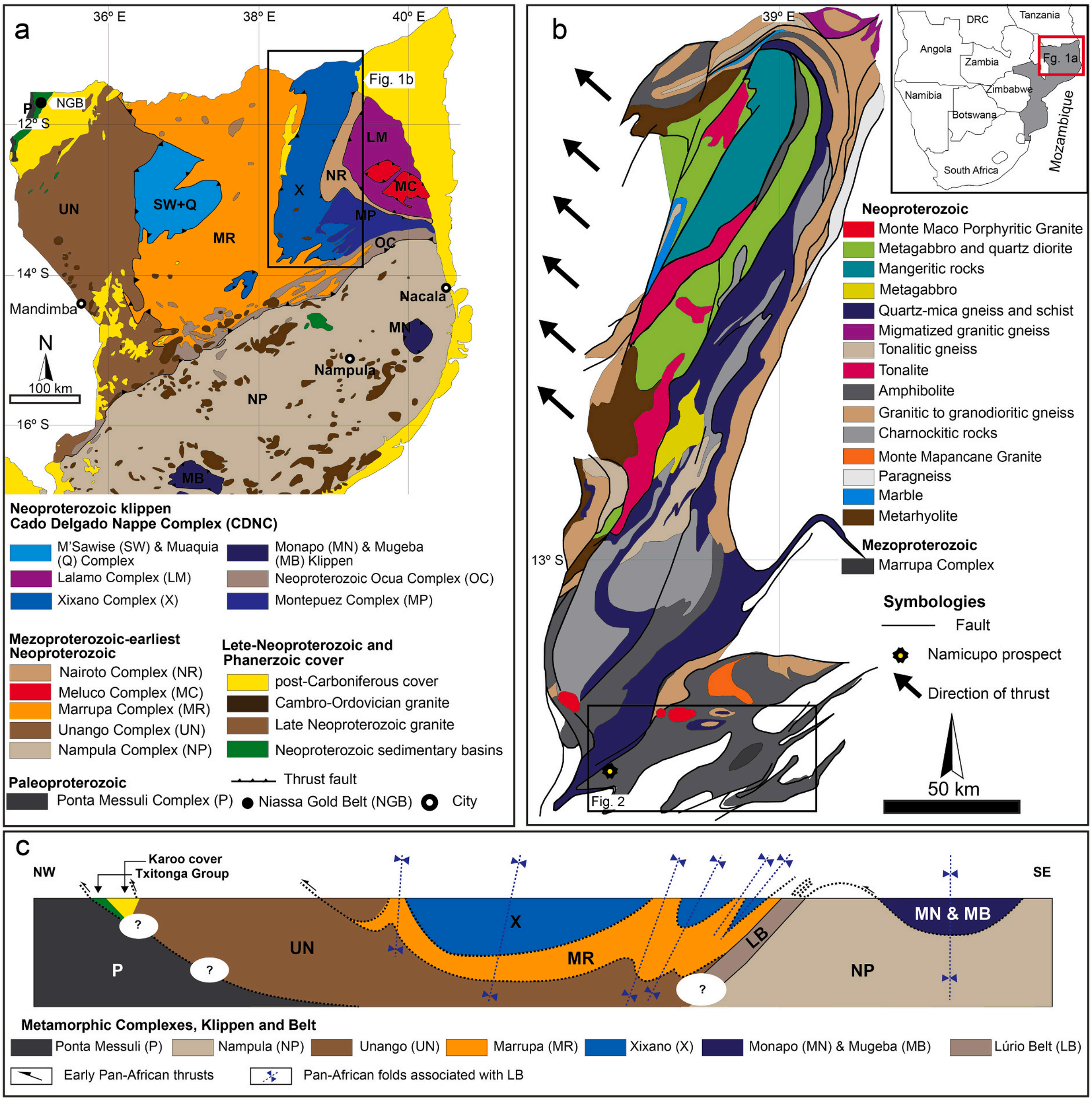

Fig. 1. (a) Regional geologic map of northeastern Mozambique (modified from Norconsult Consortium, 2007; Viola et al., 2008; Macey et al., 2013). (b) Geology of the Xixano Metamorphic Complex. (c) Schematic geological cross-section of the northeastern Mozambique terrane. The cross-section is not to scale, with no reference to the exact location, aiming to simply illustrate the laying of the metamorphic complexes and the tectonic contacts between the complexes in the region (modified from Viola et al., 2008).

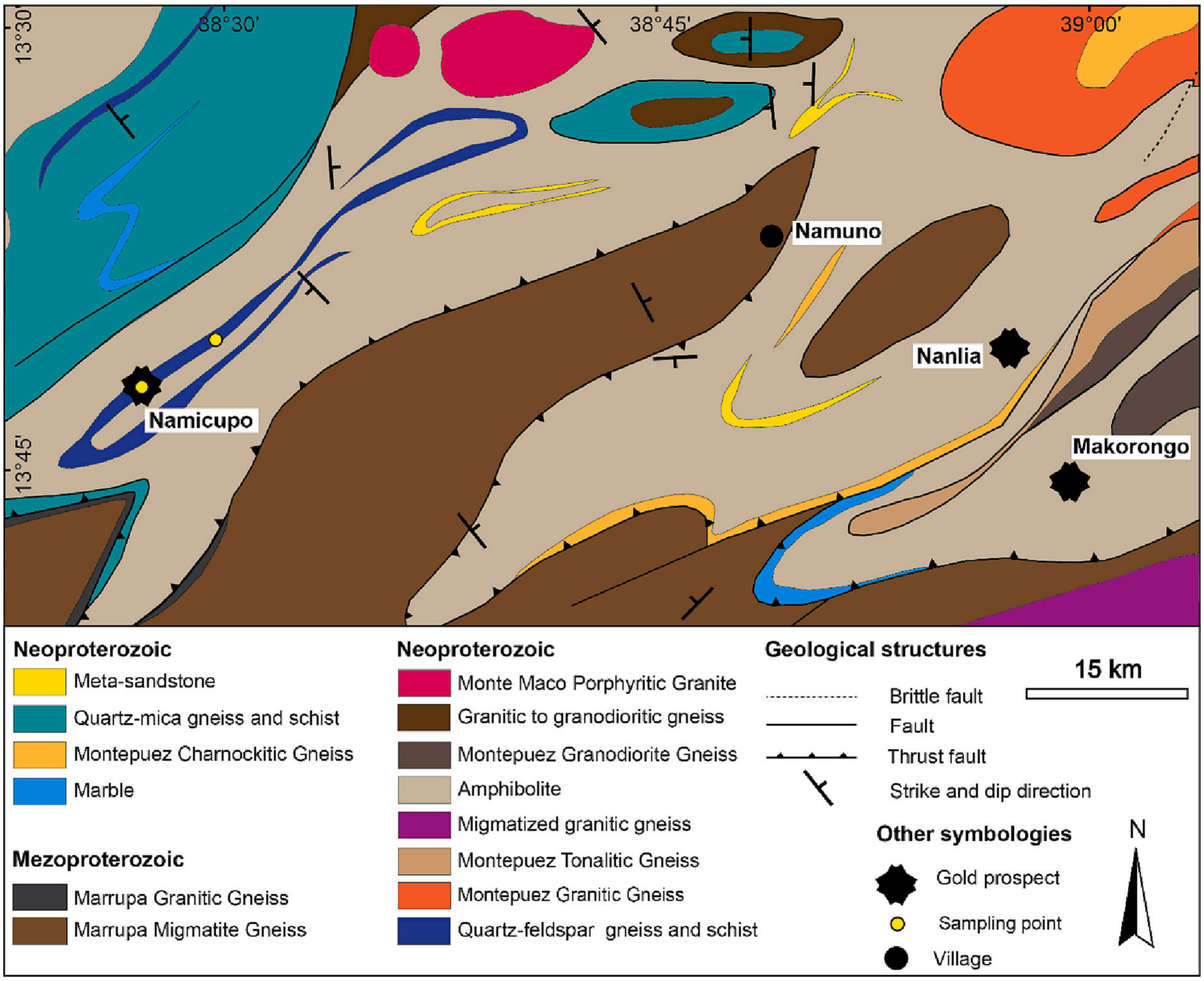

Fig. 2. Geologic map of the study area showing the location of the Namicupo prospect and other two prospects in the study area (Nanlia and Makorongo prospects; Nopeia et al., 2021), and the sampling points (modified from Norconsult Consortium, 2007).

2. Geologicals background

2.1. Regional geology and tectonic setting

The geology of northeastern Mozambique was remapped at 1:250,000 scale by Norconsult Consortium, and partly by the Council for Geoscience of South Africa, during a five-year Geological Infrastructure Development Program financed by the Nordic Development Fund and the World Bank (Norconsult Consortium, 2007; Viola et al., 2008). The region is located in the Mozambique Belt, made up of Precambrian to Cambrian high-grade ortho- and paragneisses and Neoproterozoic to Cambrian intrusive rocks (Boyd et al., 2010; Norconsult Consortium, 2007).

The northeastern terrane of Mozambique consists of two tectonic blocks separated by WSW-ENE trending late Neoproterozoic Lurio Belt which is represented by the Ocua Complex (Fig. 1a; Jamal, 2005; Norconsult Consortium, 2007; Engvik et al., 2007; Viola et al., 2008; Boyd et al., 2010; Grantham et al., 2013; Macey et al., 2013). The Nampula Block, lying to the south of the Lurio Belt, consists of orthogneisses and highly metamorphosed metasedimentary rocks dated at ca. 1150–1070 Ma (Norconsult Consortium, 2007; Bingen et al., 2009; Macey et al., 2013). The Mesoproterozoic Marrupa, Nairoto and Meluco Complexes, dominated by orthogneisses of felsic to intermediate compositions, form the basement of the terrane to the north of the Lurio Belt, and are overlain by more juvenile complexes, including the Xixano, Muaquia, M'Sawize, Lalamo and Montepuez Complexes (Fig. 1a–b; Norconsult Consortium, 2007; Boyd et al., 2010; Macey et al., 2013).

The contact between the Mesoproterozoic basements and the overlying Neoproterozoic Xixano, Muaquia, M'Sawize, Lalamo and Montepuez Complexes is characterized by thrust faults (Fig. 1a, c; Norconsult Consortium, 2007). The overlying complexes constitute what is referred to as the Cabo Delgado Nappe Complex (CDNC), interpreted to be an allochthonous domain transported northwestwards during the late Neoproterozoic to Cambrian Pan-African Orogeny, and later intruded by several suites of Cambrian late- to post-tectonic granitoids (Fig. 1a, c; Viola et al., 2008; Boyd et al., 2010; Itano et al., 2016). The CDNC and Mesoproterozoic basements were subsequently sheared and folded against the Lurio Belt in the south by a late Pan-African deformation event (Fig. 1c; Viola et al., 2008). A rapid near-isothermal decompression and subsequent cooling after high-grade metamorphism were recorded in granulite of the Lurio Belt and interpreted to have affected the CDNC (Jamal, 2005; Engvik et al., 2007).

2.2. Local geology

The Namicupo prospect is hosted by the Xixano Complex, which is a nearly NNE-SSW-trending tectonic unit thrusted over the Marrupa Complex to the west (Fig. 1b; Norconsult Consortium, 2007; Viola et al., 2008). The Xixano Complex consists of a variety of metasedimentary rocks which envelop predominantly mafic igneous rocks and granulites (Fig. 1b; Norconsult Consortium, 2007). The main rock units in the study area include amphibolite, marble and paragneiss (i.e., quartz-mica gneiss and schist, quartz-feldspar gneiss, and metasandstone) deposited at ca. 850–750 Ma (Fig. 2; Norconsult Consortium, 2007; Melezhik et al., 2008). These rocks are characterized by late Neoproterozoic amphibolite facies metamorphism (Norconsult Consortium, 2007; Melezhik et al., 2008; Viola et al., 2008; Boyd et al., 2010; Macey et al., 2013).

The gold mineralization in the Namicupo prospect is present as quartz veins hosted by well-foliated, locally weathered paragneiss and schist (Fig. 2). The mineralized quartz veins are emplaced parallel to the S1 foliation of these rocks. Gold exploitation in the Namicupo prospect is limited to unregulated artisanal mining; the annual gold production was estimated to be approximately 10 kg (Nopeia et al., 2022). The mining environment at the prospect is characterized by deep shafts and tunnels that follow the mineralized veins (Nopeia et al., 2022).

3. Samples and methods

The artisanal mining area at Namicupo is centered at coordinates S13° 40′ 58.5″ and E38° 28′ 34.2″ (Fig. 2). The mineralized quartz veins are mined by artisanal miners from shafts of about 15 m depth on average. Representative ore and host rock samples were mainly collected from the ore pile on the surface, resulting from the mining excavation. Some host rock samples were collected from outcrops at and near the mining area (Fig. 2).

Detailed petrographic analysis of representative samples of host rocks and ores was carried out using a NIKON ECLIPSE LV100N POL polarizing microscope, and a Hitachi High-Technologies SU3500 scanning electron microscope attached with an EDAX Octane Plus energy dispersive spectroscope (SEM-EDS), at the Center of Advanced Instrumental Analysis, Kyushu University. Mineral chemical analysis of pyrite, chalcopyrite and electrum was conducted using a JEOL JXA-8230 electron probe microanalyzer (EPMA) under 20 kV of acceleration voltage and a 20 nA beam current at Akita University. For the sulfides, a peak/background counting time of 20/10 s was applied for Fe, 40/20 s for Pb and Ni, 50/25 s for As, Se, Sb, Te, Bi, Cu, Zn and Co, 100/50 s for Ag and 300/150 s for Au. The standards used included FeS_2 for S and Fe, PbS for Pb, GaAs for As, Cu for Cu, Co for Co, Ni for Ni, ZnS for Zn, Au for Au, Ag for Ag, Te for Te, Sb for Sb, Bi_2S_3 for Bi, and SnSe for Se. For the electrum, a peak/background time of 20/10 s was applied for Au and Ag, 50/25 s for S, and 80/40 s for Hg and Cu. The standards used included Au for Au, Ag for Ag, FeS_2 for S, HgS for Hg and Cu for Cu.

Doubly polished wafers (100–300 μm thick) of mineralized quartz vein samples were prepared to examine the characteristics of fluid inclusions. Selected doubly polished wafers were subjected to fluid inclusion microthermometry using a Linkam LK600 heating–freezing stage attached to a Nikon Y-IM microscope at Department of Earth Resources Engineering of Kyushu University. Temperatures were calibrated using the melting temperature of synthetic substances, nonane (−51.0 °C), dodecane (−9.6 °C), tridecane (−5.5 °C), pure water (0 °C), dodecanediol (+82.0 °C), benzanilide (+166.0 °C), and sodium nitrate (+306.8 °C). The salinity of aqueous inclusions was calculated from the ice-melting temperature, using the equation of Bodnar (1993), and that of aqueous-carbonic inclusions was calculated from clathrate melting temperature using the equation of Bozzo et al. (1975). Other fluid inclusion properties (e.g., density, and molar fractions) were determined using the BULK computerized program contained in FLUIDS 1 package (Bakker, 2003; Bakker and Brown, 2003). The equation of state of Duschek et al. (1990) was applied for CO_2-rich fluid inclusions, and that of Zhang and Frantz (1987) for aqueous fluid inclusions.

The compositions of fluid inclusions were determined using a Renishaw neon laser ($\lambda = 532$ nm) Raman spectrometer attached to an optical microscope at Akita University. The Raman spectrum was calibrated using a silicon standard. Laser power was set to 50 and 100 %, with 1 and 3 s of exposure time for measurements.

About 20 mg of 11 separates of pyrite and chalcopyrite from two samples of crushed mineralized quartz veins were decomposed by a mixture of 20 mL 16 N HNO_3 and 2 mL Br_2 at 90 °C for sulfur isotope analysis. The acidified solution of samples was passed through a cation exchange column to remove cations that could co-precipitate with $BaSO_4$; 10 mL of 10 % $BaCl_2$ solution was added to the eluent to precipitate $BaSO_4$. The $BaSO_4$ obtained from pyrite and chalcopyrite were packed with V_2O_5 in tin foil (e.g., Yanagisawa and Sakai, 1983), and their sulfur isotopic ratios were determined using a Thermo Fisher Scientific Delta-V Advantage mass spectrometer, with Thermo Fisher Scientific Flash 2000 Elemental Analyzer at Akita University. The IAEA international standards NBS-127 ($\delta^{34}S_{CDT} = +20.3$ ‰), SO-5 (+0.5 ‰), and SO-6 (−34.1 ‰) were used. The isotopic ratios are reported in the standard $\delta^{34}S_{CDT}$ notation as per mil (‰) deviations from the Vienna Canyon Diablo Troilite (CDT) standard. More details of the procedure are explained in Manalo et al. (2018).

Oxygen isotope analysis of three quartz crystals from the mineralized vein samples was conducted by the commercial laboratory Activation Laboratories (Actlabs), Canada. Quartz crystals were reacted with BrF_5 at ~650 °C in nickel reaction tubes, following the procedures described in Clayton and Mayeda (1963), to convert O in quartz to O_2 gas, which was subsequently converted to CO_2 gas using a hot C rod. Isotopic analysis was performed on a Finnigan MAT Delta, dual inlet, isotope ratio mass spectrometer. The data are reported in the standard $\delta^{18}O_{SMOW}$ notation as per mil (‰) deviations from Vienna Standard Mean Ocean Water (SMOW). The external reproducibility is ±0.19 ‰.

4. Results

4.1. Petrography of host rocks

The mineralized veins in the Namicupo prospect are hosted by metasedimentary rocks, which are classified as quartz-feldspar gneiss and schist (Fig. 3a–b). The quartz-feldspar gneiss is composed of preferentially oriented biotite and muscovite, and granoblastic domains of plagioclase, K-feldspar, and quartz (Fig. 3c). Quartzite layers up to 1.5 mm thick are also observed in the quartz-feldspar gneiss (Fig. 3d). The quartz-feldspar schist consists mostly of preferentially oriented muscovite, biotite, and epidote and granoblastic domains of quartz and feldspar, with minor iron oxyhydroxide replacing biotite and muscovite. Inclusions of apatite and titanite in biotite are commonly observed (Fig. 3e). The common feldspar minerals in the quartz-feldspar schist are sodic plagioclase and microcline; micro perthite exsolution texture made of albite and microcline are commonly observed (Fig. 3f).

The peak metamorphic assemblage of metasedimentary host rocks at the Namicupo prospect is represented by quartz-K-feldspar-muscovite-biotite-plagioclase-titanite. On the basis of its mode of occurrence (i.e., replacing biotite and muscovite), epidote could represent a retrograde phase, and goethite likely resulted from weathering. This peak mineral assemblage is indicative of relatively high pressure and temperature metamorphism, at amphibolite facies conditions (e.g., Norconsult Consortium, 2007; Spear, 1993).

4.2. Ore mineralogy

4.2.1. Mineralized quartz veins and ore mineral assemblage

The gold mineralization in the Namicupo prospect occurs as quartz veins emplaced parallel to the S1 foliation of the metasedimentary host rocks (Fig. 4a). The collected mineralized vein samples, composed mainly of quartz and sulfides, are characterized by small voids partially filled by oxides and oxyhydroxides, suggesting leaching or oxidation of pre-existing primary sulfides (Fig. 4a). The quartz vein consists of a primary mosaic quartz (quartz 1) exhibiting a dissolution and recrystallization texture at the edges, represented by fine-grained and radial quartz bands (quartz 2) surrounding primary grains (Fig. 4b).

The ore mineral assemblage comprises electrum (in this study, electrum is used in sensu lato, to refer to Au-Ag alloy with variable Ag content, including lower than 20 at.%), pyrite, chalcopyrite, galena, spionkopite ($Cu_{1.4}S$), minium, hematite, goethite, covellite, chalcocite,

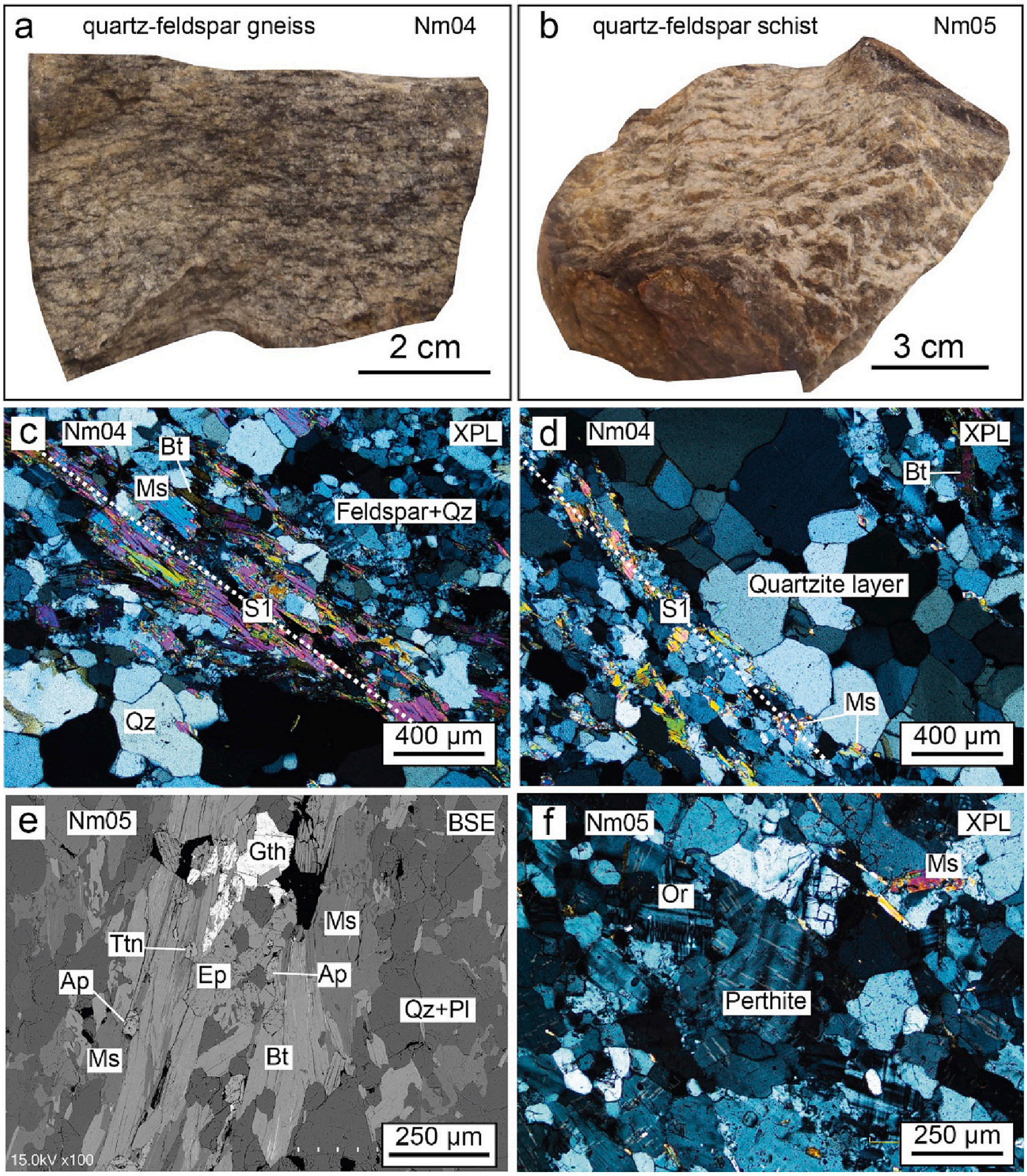

Fig. 3. (a) Hand sample of foliated quartz-feldspar gneiss. (b) Hand sample of strongly foliated and weathered quartz-feldspar schist. (c and d) Photomicrographs of quartz-feldspar gneiss showing (c) preferentially oriented biotite and muscovite and granoblastic domains of quartz and feldspar, and (d) quartzite layer parallel to the S1 foliation. (e and f) Photomicrographs of quartz-feldspar schist showing (e) epidote and goethite overgrowing biotite and muscovite and (f) perthite texture of feldspar. Abbreviations: Ap – apatite, BSE – backscattered electron image, Bt – biotite, Ep – epidote, Gth – goethite, Ms. – muscovite, Or – orthoclase, Pl – plagioclase, Qz – quartz, Ttn – titanite, XPL – crossed polarized light.

barite, anglesite ($PbSO_4$), and cerussite ($PbCO_3$; Fig. 4c–e). Pyrite is the main sulfide and is associated with chalcopyrite and electrum, sporadically partially replaced by goethite and hematite (Fig. 4c, d, f). Chalcopyrite is also associated with pyrite and electrum, often replaced by chalcocite and covellite along the grain boundaries (Fig. 4c, g). Goethite and hematite commonly replace pyrite and occur in association with barite (Fig. 4c–d), while cerussite, anglesite, and minium occur as products of partial or total replacement of galena (Fig. 4e). Electrum is either associated with primary sulfides or coexists with goethite, minium and barite. The grain size of electrum coexisting with pyrite and chalcopyrite is <25 μm (Fig. 4f–g). On the other hand, electrum associated with goethite, minium and barite is anhedral to subhedral, with grain size of 50 μm on average, and occurs commonly enveloped by or intergrown with these minerals (Fig. 4d, h, i).

4.2.2. *Ore mineral chemistry*

4.2.2.1. Electrum. Results of the major and trace element analyses of electrum, including Ag, Hg, S and Cu, are shown in Table 1. Electrum in the Namicupo prospect occurs either associated with pyrite and chalcopyrite (Fig. 4f, g), or intergrown with barite, goethite, and minium (Fig. 4d, h, i). These two different textural types of electrum are characterized by distinct chemical compositions. SEM-EDS semiquantitative analysis revealed that the electrum intergrown with pyrite and chalcopyrite contains 15–26 at.% Ag (Fig. 4f, g, j); while that coexisting with barite, goethite and minium contains higher Ag contents of 39–46 at.% (Fig. 4d, h, j). EPMA analysis revealed that the Au-rich electrum has Hg and Cu contents of 1300 and 700 ppm on average, respectively, with no S (Table 1). On the other hand, the Ag-rich electrum is characterized by relatively higher Hg of 2500 ppm on average, and high S contents up to 1200 ppm, but no Cu (Table 1).

On the basis of the ore mineral paragenesis and the chemistry of electrum, the gold mineralization in the Namicupo prospect can be divided into two stages. The Stage I, considered to be primary mineralization, is represented by Au-rich electrum coexisting with pyrite and chalcopyrite. The Stage II is characterized by Ag-rich electrum intergrown with goethite, minium, and barite, which replaced primary sulfides (Fig. 5).

4.2.2.2. Pyrite and chalcopyrite. Representative elemental compositions of pyrite and chalcopyrite coexisting with Au-rich electrum are shown in Table 2. Pyrite shows homogenous distribution of trace elements such as

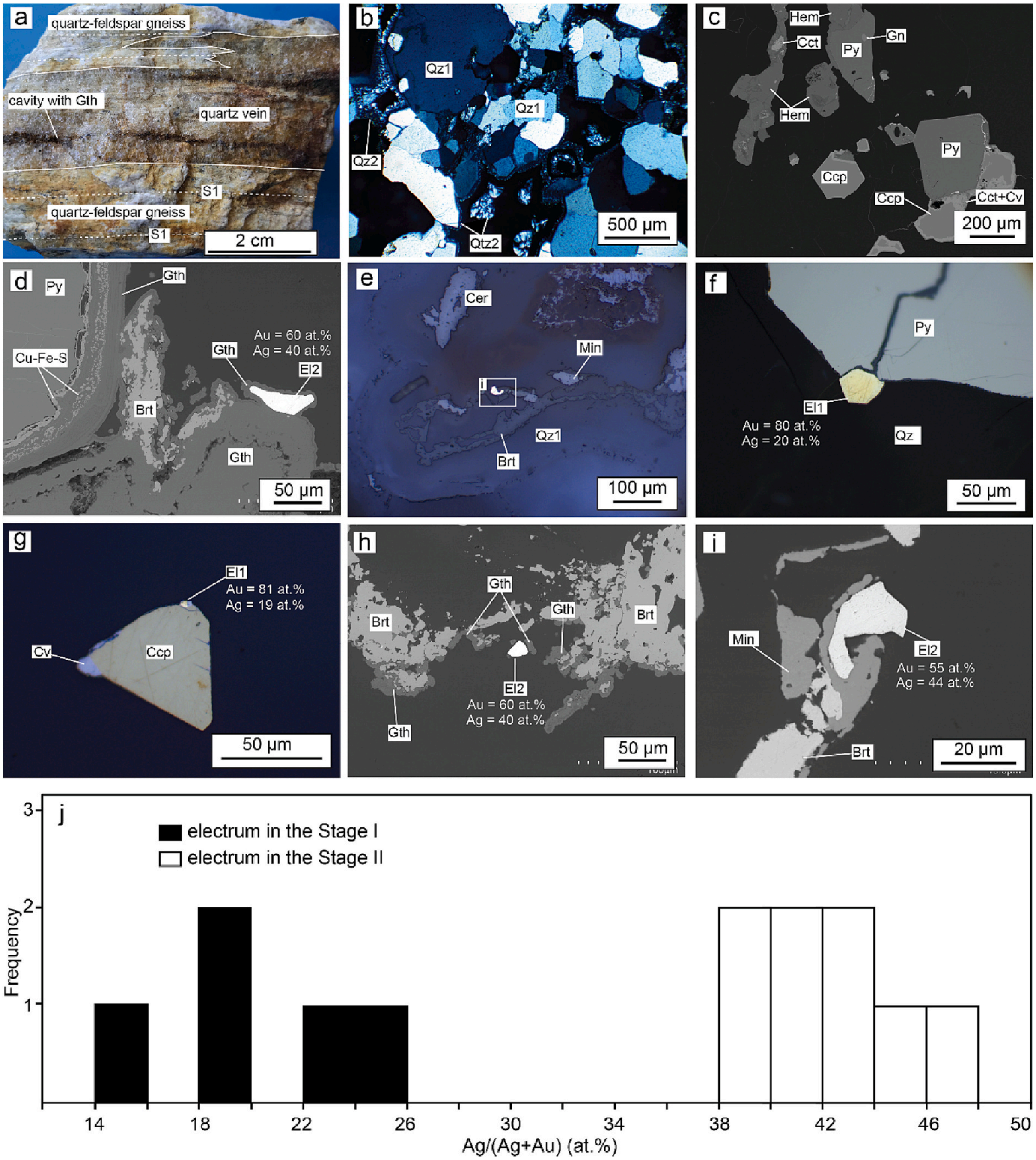

Fig. 4. (a) A hand sample of quartz vein emplaced parallel to the S1 foliation of quartz-feldspar gneiss, with some cavities filled up with iron oxyhydroxide. (b) A crossed polarized light image showing mosaic primary quartz surrounded by a late-formed fine-grained (occasionally radial) quartz. (c) A backscattered electron (BSE) image showing pyrite and chalcopyrite partially replaced by hematite, and chalcocite and covellite, respectively. (d) A BSE image showing goethite, which replaced pyrite, enveloping Ag-rich electrum. (e) A reflected light (RL) photomicrograph showing cerussite, barite and minium in association with Ag-rich electrum. (f) A RL photomicrograph showing a grain of Au-rich electrum coexisting with pyrite. (g) A RL photomicrograph showing primary Au-rich electrum associated with chalcopyrite. (h) A BSE image showing Ag-rich electrum intergrown with goethite and barite. (i) A BSE image showing Ag-rich electrum enveloped by minium and barite. (j) Histograms of Ag contents of electrum from Stage I and Stage II. Abbreviations: Brt– barite, Cer – cerussite, Ccp – chalcopyrite, Cct – chalcocite, Cv – covellite, El1 – Au-rich electrum coexisting with pyrite and chalcopyirite, El2 – Ag-rich electrum coexisting with barite, minium and goethite, Gn – galena, Gth – goethite, Hem – hematite, Min – minium, Py – pyrite, Qz1 – primary quartz, Qz1 – late-formed quartz.

Se, Co, Ni, As, Ag, Cu and Zn, with contents of these elements generally below 1 wt% (Fig. 6a). Arsenic contents of pyrite are up to 800 ppm, Au contents reach 500 ppm, and Ag, Pb, and Bi are generally below the detection limit (Fig. 6a; Table 2). The Co contents of pyrite are up to 0.7 wt%; the Co/Ni ratios are between 0.1 and 10 (Fig. 6b). Compared to pyrite, chalcopyrite has similar Au (up to 500 ppm) and is more enriched in Ag and Zn, with Ag contents reaching 1600 ppm (Fig. 6a). The Pb, Te, and Bi contents of chalcopyrite are generally below the detection limit (Fig. 6a; Table 2).

4.3. *Fluid inclusions*

4.3.1. *Petrography*

Doubly polished wafers of mineralized quartz vein samples were

Table 1
Representative chemical composition data of electrum.

Sample ID	Nm02						
Spot ID	Stage I electrum			Stage II electrum			dl (ppm)
	G1_1	G1_2	G1_4	G3_1	G3_2	G3_4	
Au (wt%)	87.93	89.41	88.04	68.17	69.46	69.48	319
Ag	10.69	9.38	11.03	30.04	29.19	29.68	103
Hg	0.17	0.16	0.09	0.17	0.24	0.27	512
Cu	0.13	0.05	0.06	0	0	0	89
S	0	0	0	0.07	0.05	0.12	30
Total	98.9	99.0	99.2	98.4	98.9	99.5	
Atomic %							
Au	81.4	83.7	81.2	55.2	56.4	55.7	
Ag	18.1	16.0	18.6	44.4	43.2	43.5	
Hg	0.2	0.1	0.1	0.1	0.2	0.2	
Cu	0.4	0.2	0.2	0	0	0	
S	0	0	0	0.3	0.2	0.6	
Total	100	100	100	100	100	100	

dl - detection limit.

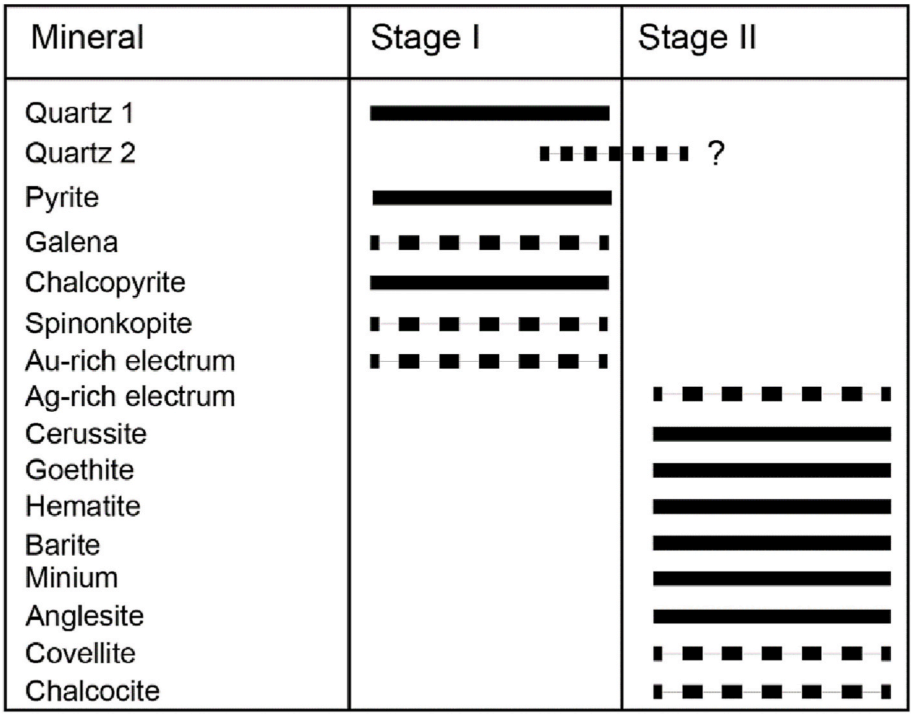

Fig. 5. Mineral paragenesis of the Namicupo prospect. Thick solid lines indicate major occurrences, and dashed lines indicate minor occurrences.

petrographically examined for fluid inclusions. Measurable fluid inclusions are observed only in primary quartz crystals (Fig. 7a). Only primary inclusions, interpreted to be entrapped during the crystallization of the host quartz (e.g., Roedder, 1984), were targeted for fluid inclusion studies. Primary inclusions occur clustered within the crystal or along crystal boundaries (Fig. 7a). On the basis of the number of phases and composition at room temperature, three types of primary fluid inclusions were identified. Type A are three-phase irregular- to oval-shaped aqueous-carbonic inclusions containing aqueous liquid, CO_2 liquid and vapor, with sizes varying from 5 to 15 μm (Fig. 7a–b). The volume of CO_2 (liquid and vapor) of Type A inclusions, at room temperature, varies from ca. 10 to ca. 30 vol%. Type B are CO_2-rich inclusions, which occur either as mono-phase (vapor or liquid) or two-phase (vapor and liquid) inclusions at room temperature (Fig. 7c–e). Size of the Type B inclusion is commonly <10 μm. The mono-phase Type B inclusions are generally dark and elongated (Fig. 7c–e). The two-phase Type B inclusions are commonly hexagonal- to rectangular-shaped and dark in appearance. The CO_2 vapor of two-phase Type B inclusions accounts for >90 vol% of the total volume, and the liquid phase occurs as a thin rim of liquid CO_2 or liquid H_2O (Fig. 7c–d). Type C inclusions are two-phase (liquid and vapor) aqueous inclusions with size <15 μm (Fig. 7a, f). The shapes of Type C inclusions vary from rounded, ovoidal to elongated. The vapor volume of Type C inclusions varies from ca. 5 to ca. 20 vol% (Fig. 7f). The three types of inclusions coexist in the same fluid inclusion assemblage indicating that these fluid types are coeval (Fig. 7f–g).

4.3.2. *Microthermometry*

Microthermometry measurement of primary inclusions was conducted on doubly polished wafers from the sample Nm02, which contains visible gold occurring as electrum and measurable fluid inclusions. The Type A aqueous-carbonic, Type B CO_2-rich and Type C aqueous inclusions were analyzed. Microthermometry measurement of Type B CO_2-rich inclusions, particularly the final melting temperature of CO_2,

Table 2
Representative EPMA analyses of pyrite and chalcopyrite.

Mineral Spot ID	S (dl, 0.01)	Fe (0.01)	As (0.02)	Se (0.02)	Co (0.01)	Cu (0.01)	Ni (0.01)	Total
Pyrite								
P2-1	52.47	45.19	bdl	bdl	0.67	0.01	bdl	98.38
P2-3	52.55	45.55	bdl	bdl	0.47	bdl	bdl	98.57
P2-5	52.60	45.54	0.01	0.04	0.34	0.02	bdl	98.57
P3-1	52.20	45.67	bdl	0.06	0.15	bdl	bdl	98.10
P3-3	52.70	45.48	0.04	0.04	0.28	0.01	0.26	98.82
P3-4	52.71	44.96	bdl	0.02	0.72	bdl	0.18	98.61
P7-1	53.18	45.62	0.05	0.04	0.20	bdl	bdl	99.10
P7-3	53.13	45.76	0.02	0.08	0.07	bdl	0.04	99.16
P7-5	52.99	45.77	bdl	0.03	0.07	bdl	0.03	98.88
P7-7	52.89	45.82	bdl	0.09	0.18	bdl	bdl	98.98
P8-1	52.65	45.58	bdl	0.04	0.08	bdl	0.20	98.56
P8-3	52.76	45.85	0.05	0.01	0.07	bdl	0.15	98.91
P8-5	52.88	45.82	bdl	0.06	0.07	bdl	0.19	99.04
P8-7	52.99	45.90	0.03	0.04	0.07	0.14	0.04	99.24
P9-2	53.15	45.82	0.05	0.07	0.13	0.01	bdl	99.25
P9-3	53.22	45.81	0.06	0.04	0.12	0.02	bdl	99.28
P9-4	53.38	45.78	0.04	0.02	0.15	0.02	bdl	99.44
P9-6	53.11	45.82	bdl	0.01	0.19	0.02	bdl	99.16
Chalcopyrite								
Cp-6-1	33.72	29.94	0.05	0.04	0.05	33.75	bdl	97.79
Cp-1-5	33.69	29.99	bdl	bdl	0.05	33.97	bdl	97.82
Cp-2-1	33.94	30.12	0.05	0.08	0.06	33.85	bdl	98.15
Cp-2-2	33.91	29.99	0.06	bdl	0.04	33.86	bdl	97.92
Cp-2-3	33.77	30.02	0.03	0.02	0.04	33.88	bdl	97.83
Cp-4-3	33.93	29.54	0.02	0.08	0.04	34.44	bdl	98.11
Cp-4-4	34.12	29.78	0.04	0.04	0.05	34.04	bdl	98.13
Cp-3-4	33.82	29.95	bdl	0.07	0.04	33.81	bdl	97.77
Cp-3-5	33.79	29.95	0.05	0.04	0.04	33.96	bdl	97.92
Cp-4-2	33.84	29.81	0.04	0.02	0.04	33.97	bdl	97.81

bdl - below the detection limit. The detection limit (number in brackets; dl) is given in wt%.

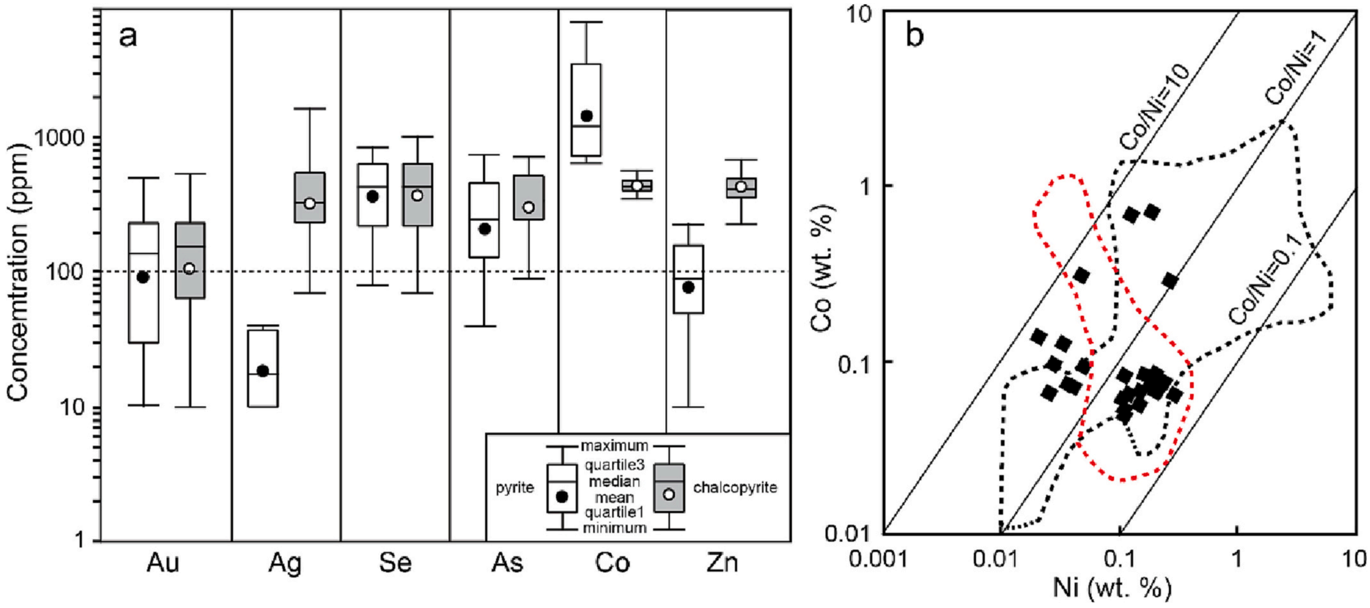

Fig. 6. Geochemical signatures of pyrite and chalcopyrite. (a) Box and whisker diagram showing concentrations of Au, Ag, Se, As, Co and Zn of pyrite and chalcopyrite. The horizontal dashed line is the average limit of detection for all elements in EPMA analysis. (b) Plots of Co vs. Ni contents of pyrite. The fields of pyrite from orogenic-type gold (red dashed curve) and volcanogenic massive sulfide (VMS) deposits (black dashed line) extracted from Reich et al. (2016; and references therein) are shown for comparison. (For interpretation of the references to colour in this figure legend, the reader is referred to the web version of this article.)

was limited to only a few number of inclusions due to the small size, and high refraction of these type of inclusions. However, since the main intent of measuring the melting temperature of CO_2-rich (or carbonic) inclusions is to check the purity of CO_2, the compositions of these inclusions were assessed through Raman spectroscopy presented in the next section, instead of the final melting temperature of CO_2. The dissolution of clathrate (T_mCl) of Type A inclusions occurred between +5.8 and +9.5 °C. The homogenization temperature of CO_2 into liquid

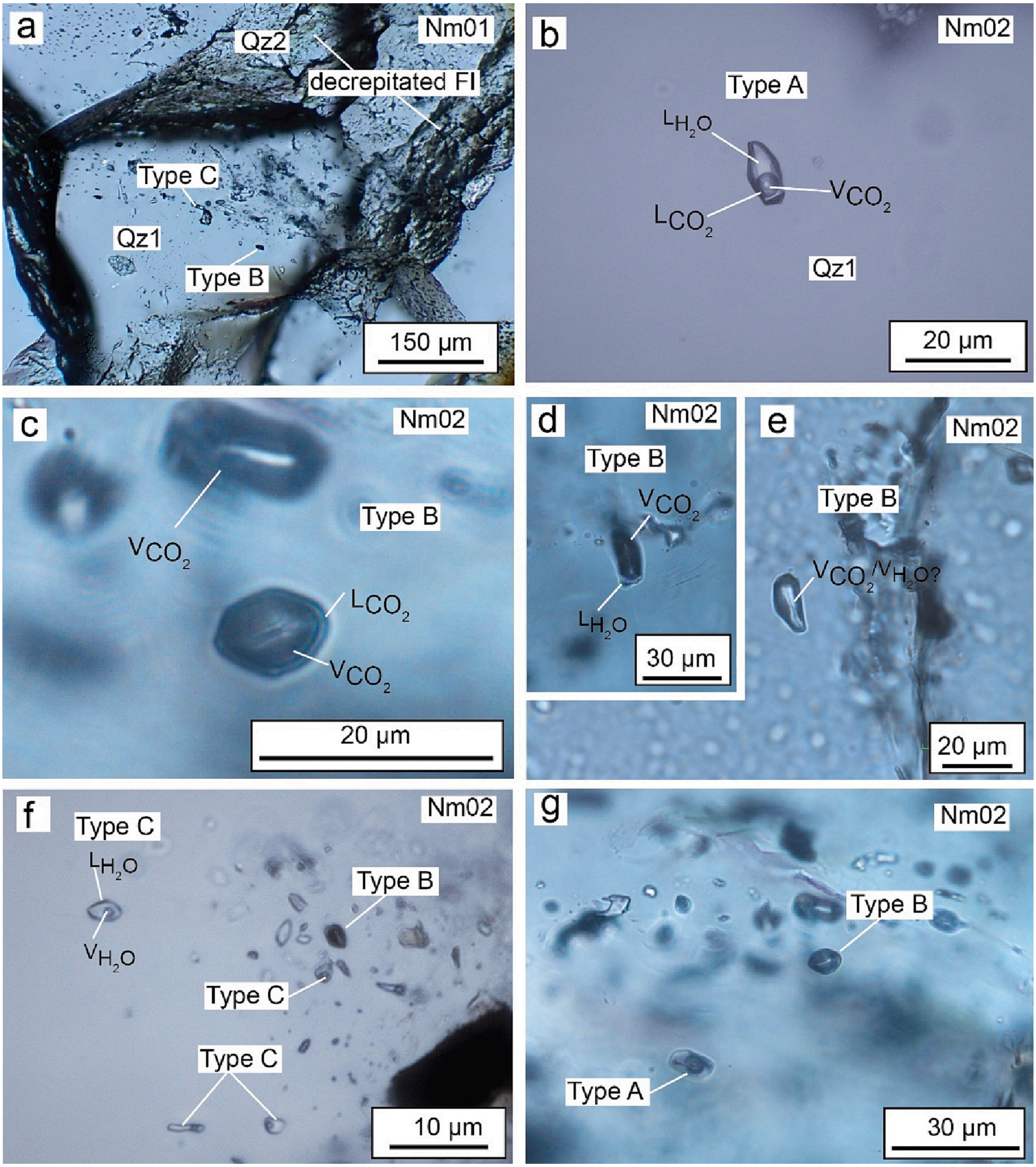

Fig. 7. Plane polarized light photomicrographs of fluid inclusions hosted in primary quartz (Qz1) crystals. (a) An extended depth of focus transmitted light image showing decrepitated inclusions in quartz 2, which gives a soiled appearance of sample. (b) A primary Type A fluid inclusion consisting of aqueous liquid, CO_2 liquid and vapor phases. (c) Primary Type B CO_2-rich fluid inclusions. (d) A primary Type B CO_2-rich inclusion consisting mainly of vapor CO_2 phase with a thin rim of liquid H_2O. (e) A primary Type B, mono-phase (vapor) fluid inclusion. (f) Coeval Type B and Type C inclusions. (g) Coexistence of Type A and Type B inclusions in the same fluid inclusion assemblage. Abbreviations: FI – fluid inclusion, Qz1 – primary quartz crystal, Qz2 – late-formed quartz band, Type A – aqueous-carbonic three-phase fluid inclusion, Type B – mono-phase or two-phase CO_2-rich fluid inclusion, Type C – two-phase aqueous fluid inclusion.

phase (T_hCO_2) of Type A inclusions varies from +26.7 to +30.5 °C (Fig. 8a). The T_hCO_2 to liquid phase of 5 Type B inclusions, which are mono-phase (liquid) at room temperature, ranges from +12.9 to +29.3 °C (Fig. 8a), corresponding to a density of 0.620–0.839 g/cm^3 (Table 3).

Most Type A inclusions did not homogenize upon heating to more than +400 °C; some decrepitated before homogenization and others experienced explosion of the aqueous liquid phase after the expansion of CO_2 gas with increasing temperature. The total homogenization temperature to liquid phase (T_h) of three Type A inclusions, however, were 140, 219 and 241 °C (Fig. 8b). The salinity of Type A inclusions was calculated from the melting temperature of clathrate (Bozzo et al.,

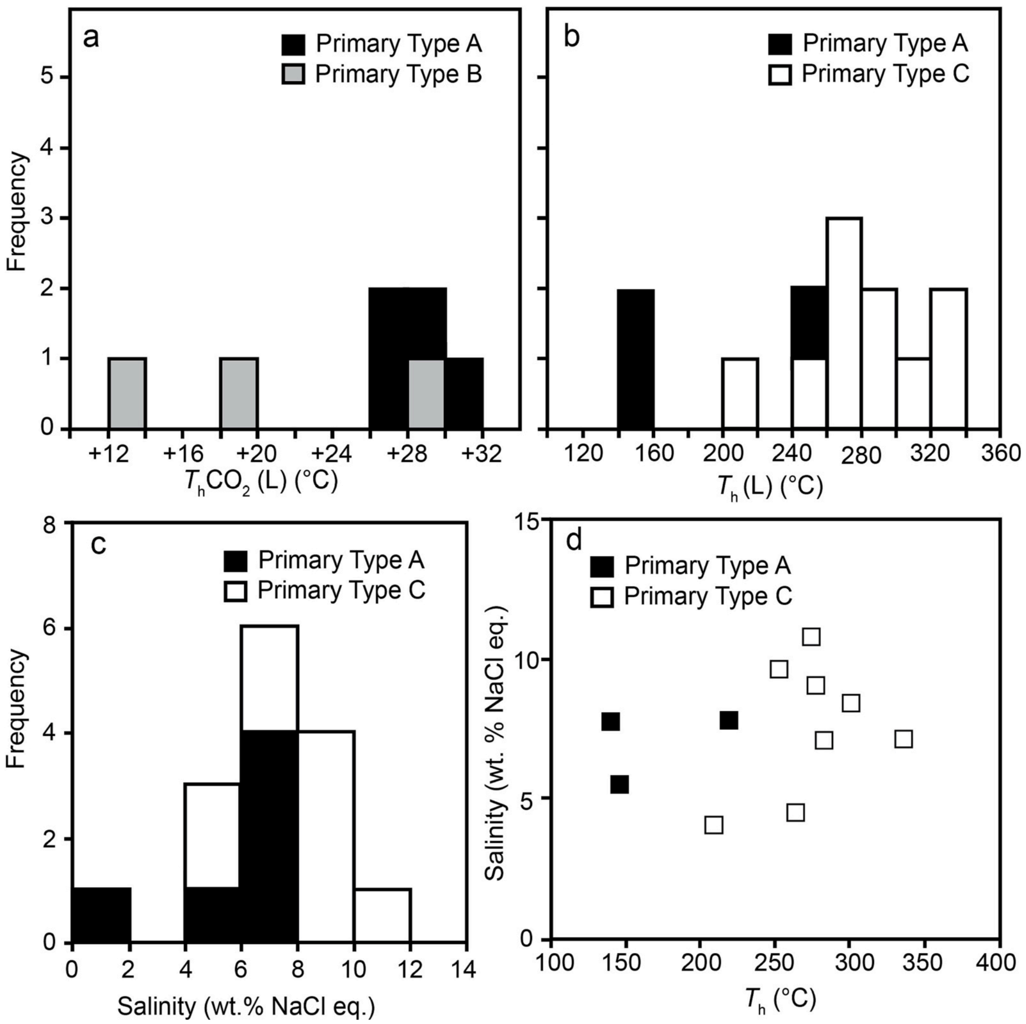

Fig. 8. Histograms of (a) homogenization temperature of CO_2 (T_hCO_2) to liquid phase of Type A and Type B fluid inclusions, (b) total homogenization temperature (T_h) to liquid phase of Type A and Type C fluid inclusions, and (c) salinity of Type A and Type C fluid inclusions calculated from melting temperature of clathrate and ice, respectively. (d) Binary plots of salinity and T_h of Type A and Type C fluid inclusions. Type A – aqueous-carbonic three-phase fluid inclusion, Type B – mono-phase or two-phase CO_2-rich fluid inclusion, Type C – two-phase aqueous fluid inclusion.

Table 3
Summary of microthermometry results of fluid inclusions.

Fluid inclusion type	Fluid system	T_mIce (°C)	T_mCl (°C)	T_h CO_2 (°C)	T_h total (°C)	Density (g/cm^3)	Salinity (wt% NaCl eq.)
Type A	H_2O-CO_2-NaCl		+5.8 to +9.5 (7)	+26.7 to +30.5 (5)	140.2 to 243.8 (3)		1.0 to 7.8 (7)
Type B	CO_2 (±N2 ± H_2O)			+12.9 to +29.3 (4)		0.620 to 0.839	
Type C	H_2O-NaCl	−7.3 and −2.4 (10)			209.2 to 337.4 (10)	0.725 to 0.889	4.0 to 10.8 (10)

1975), between 1.0 and 7.8 wt% NaCl eq. (Fig. 8c). Regarding the Type C aqueous inclusions, the T_h to liquid phase varies from 209 to 337 °C (Fig. 8b). The final melting temperature of ice (T_mIce) of this type of inclusions ranges from −7.3 to −2.4 °C, corresponding to salinity of 4.0 to 10.8 wt% NaCl eq. (Fig. 8c). The density of aqueous inclusions calculated from the T_h varies from 0.725 to 0.889 g/cm^3 (Table 3). Binary plots show no correlation between salinity and homogenization temperature of Type A and Type C inclusions (Fig. 8d).

4.3.3. Laser Raman spectroscopy

The compositions of fluid inclusions were assessed by Raman spectroscopy. The Raman spectra of gas phases of Type A inclusions showed prominent peaks at approximately 1280 and 1385 cm^{-1} assigned to $v1$ and $v2$ vibration bands of CO_2, respectively, and a weak broad band of water between approximately 3100 and 3700 cm^{-1} (Fig. 9a–b). An inconspicuous peak at around 2330 cm^{-1} was identified as trace of N_2 gas (Fig. 9a). The spectrum of the liquid phase of Type A inclusions is characterized mainly by a very prominent broad band of H_2O (Fig. 9c). The gas phase of Type C aqueous inclusions showed a prominent broad band of H_2O, with no CO_2 or any other gases (Fig. 9d).

Representative Raman spectra of Type B CO_2-rich inclusions are presented in Fig. 10. Type B inclusions occur either as mono-phase (vapor or liquid) or two-phase (mainly vapor and a very thin rim of liquid phase) under transmitted light microscopy at room temperature. The Raman spectrum of a dark mono-phase inclusion showed prominent peaks of CO_2 (1283 and 1385 cm^{-1}), and a minor peak at 2326 cm^{-1} assigned to N_2 gas (Fig. 10a). A spectrum acquired along the rim of an apparently mono-phase inclusion showed a prominent H_2O peak (probably H_2O gas) at around 3766 cm^{-1} (Fig. 10b). All the analyzed Type B inclusions showed a weak H_2O band at around 1635 cm^{-1}, suggesting that these inclusions contain small amount of H_2O. We also observed a strong peak at 1078 cm^{-1}, in a Type B inclusion, probably a daughter mineral of natrite (Na_2CO_3; Fig. 10c). This daughter mineral in the inclusions was not observed under the microscope due to the dark appearance of the Type B inclusions.

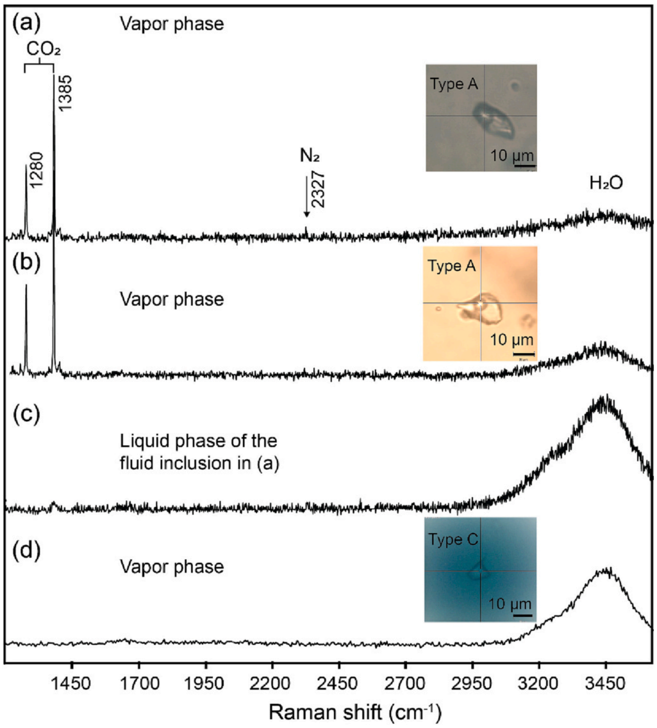

Fig. 9. Raman spectra of (a and b) gas phase and (c) liquid phase of Type A aqueous-carbonic inclusions, and (d) gas phase of a Type C aqueous inclusion.

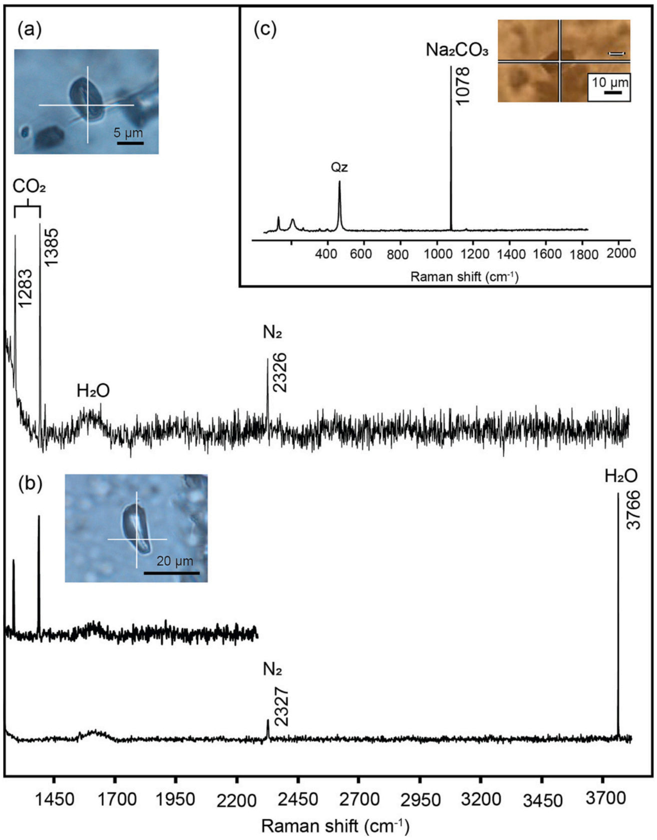

Fig. 10. Raman spectra of Type B CO_2-rich inclusions. (a) A mono-phase vapor inclusion composed mainly of CO_2 with minor N_2. (b) A mono-phase CO_2-rich inclusion with vapor H_2O. (c) A daughter mineral, natrite (Na_2CO_3), hosted in a CO_2-rich inclusion. Abbreviation: Qz – quartz.

4.4. *Sulfur and oxygen isotopes*

Pyrite and chalcopyrite associated with Stage I gold mineralization were separated from the quartz veins for S-isotope analysis. The sulfur isotopic ratios ($\delta^{34}S_{CDT}$) of pyrite and chalcopyrite vary in a narrow range, from −3.5 to +0.9 ‰ (Table 4). The oxygen isotopic ratios ($\delta^{18}O_{SMOW}$) of three samples of quartz extracted from the mineralized veins are +3.6, +5.3, and +7.1 ‰ (Table 4).

5. Discussion

5.1. *Primary mineralization*

Primary gold mineralization in the Namicupo prospect is represented by Au-rich electrum (with Ag contents varying between 15 and 26 at.%), intergrown with pyrite and chalcopyrite (Fig. 5). Trace elements in sulfides and electrum can be incorporated by isomorphic substitution into the crystal lattice or as nano-scale inclusions during the formation of these minerals; therefore, they may be an indicator of the origin of hosting minerals (Reich et al., 2005, 2016; McInnes et al., 2008; Agangi et al., 2014; Li et al., 2018). The intergrowth texture between the Au-rich electrum with pyrite and chalcopyrite suggests that the Au-rich electrum is cogenetic with primary sulfides. Cobalt and Ni ratios in pyrite have long been used as proxy for pyrite origin, whereby high Co/Ni ratios are attributed to hydrothermal-magmatic systems, in contrast to sedimentary environments characterized by lower Co/Ni ratios (Bralia et al., 1979; Reich et al., 2016). The Co/Ni ratios of pyrite in the Namicupo prospect are usually >0.1, and vary widely, which is consistent with pyrite derived from hydrothermal process, similar to those of several hydrothermal orogenic-type gold deposits (e.g., Fig. 6b; Reich et al., 2016 and references therein).

5.1.1. *Nature and entrapment P-T conditions of fluids*

The coexistence of CO_2-rich (carbonic), aqueous-carbonic, and aqueous inclusions in the same quartz crystal (Fig. 7a, f, g) suggests a heterogeneous entrapment of fluids. Heterogeneous entrapment can be an evidence of fluid immiscibility (Ramboz et al., 1982). Fluid

Table 4
Sulfur and oxygen isotopic ratios of primary mineralization.

Sample	Mineral	$\delta^{34}S_{CDT}$ (‰)	$\delta^{18}O_{SMOW}$ of quartz (‰)	Temperature (°C)	$\delta^{18}O_{SMOW}$ of water (‰)
Nm01-2	Pyrite	−3.5			
Nm01-3	Pyrite	−3.1			
Nm01-4	Pyrite	−2.9			
Nm01-5	Pyrite	−3.2			
Nm07-1	Chalcopyrite	+0.9			
Nm07-2	Pyrite	−0.2			
Nm07-3	Pyrite	0.0			
Nm07-4	Pyrite	0.0			
Nm07-5	Pyrite	+0.2			
Nm07-6	Pyrite	−0.1			
Nm01	Quartz		+7.1	375	+2.5
Nm02	Quartz		+3.6		−1.0
Nm03	Quartz		+5.3		+0.7

$\delta^{18}O_{SMOW}$ of water were calculated on the basis of average temperature estimated from intersection of isochores, assuming isotopic equilibrium between H_2O and SiO_2 (e.g., Clayton et al., 1972).

immiscibility in the Namicupo prospect is also supported by the variable degree of vapor filling, as well as the presence of natrite (Na_2CO_3) daughter mineral in CO_2-rich inclusions as revealed by Raman spectroscopy (Fig. 10c). Natrite is a sodium carbonite (Khomyakov, 1983), which could have been precipitated from an initial H_2O-CO_2-NaCl fluid during entrapment of fluids. Therefore, the Type B CO_2-rich and Type C aqueous inclusions could represent two end members separated from a single primary and homogeneous fluid, represented by the Type A aqueous-carbonic fluid inclusions. On the basis of the compositions of the three types of inclusions, dominated by H_2O and CO_2, with minor N_2, and salinity of <11 wt% NaCl eq., the parental fluid belonged to the H_2O-CO_2-NaCl fluid system. This fluid system is generally associated with a metamorphic fluid source responsible for orogenic-type gold deposits (e.g., Schmidt Mumm et al., 1997; Mishra and Panigrahi, 1999; Wilkinson, 2001; Goldfarb et al., 2005; Phillips and Powell, 2010; Goldfarb and Groves, 2015).

The isochore intersection method was employed for coexisting primary CO_2-rich Type B and aqueous Type C inclusions, under the assumption that these inclusion types were separated from a single primary fluid through fluid immiscibility (e.g., Roedder and Bodnar, 1980). Isochores of fluid inclusions were calculated using ISOC (for aqueous inclusions) and LonerSpW (for CO_2-rich inclusions) computer programs provided by the FLUIDS 1 package (Bakker, 2003). The equation of state of Span and Wagner (1996) and that of Zhang and Frantz (1987) were applied for Type B and Type C inclusions, respectively. Isochores of the highest, average, and lowest densities of coexisting Type B and Type C inclusions were plotted in the P-T diagram (Fig. 11). The minimum intersecting temperature is 250 °C and the maximum is above 600 °C (Fig. 11). Isochore intersecting pressure varies from approximately 65 to 310 MPa (Fig. 11). The intersection of isochores of average density of carbonic inclusion and aqueous inclusion, at 375 °C and 175 MPa, could represent the approximate average trapping temperature and pressure conditions of fluid inclusions. The average pressure value of 175 MPa corresponds to an entrapment depth of 6.6 km, assuming an overlying rock density of 2.7 g/cm^3, under the lithostatic pressure condition. These values are assumed to represent the P-T-depth conditions of fluid immiscibility, and can be interpreted as the approximate formation temperature, pressure, and depth conditions of primary gold mineralization in the Namicupo prospect.

5.1.2. Implications of sulfur and oxygen isotopes

The origin of ore-forming fluids in orogenic gold deposits has been discussed by many researchers, but remains enigmatic (Ridley and Diamond, 2000; Goldfarb et al., 2005; Phillips and Powell, 2010; Goldfarb and Groves, 2015; Malta et al., 2020). In general, stable isotope signatures are useful tracers for the source of ore-forming fluids (Ohmoto, 1986; Goldfarb and Groves, 2015; Chai et al., 2017). Interpretation of stable isotope data of gold deposits hosted in metamorphic terranes, however, is not straightforward and is hampered by a number of problems including the (1) fluid-rock interaction along the flow path and the sites of ore deposition, (2) overlap of isotopic values for different sources, and (3) the uncertainties in permissive isotopic ranges for a specific source (Goldfarb and Groves, 2015). The sulfur isotopic ratios ($\delta^{34}S_{CDT}$) of pyrite and chalcopyrite associated with Au-rich electrum vary between −3.5 and +0.9 ‰, and the oxygen isotopic ratios ($\delta^{18}O_{SMOW}$) of water calculated from those of quartz at a temperature of 375 °C, estimated from intersecting average density isochores, assuming oxygen isotopic equilibrium between H_2O and SiO_2 (e.g., Clayton et al., 1972) are −1.0, +0.7, and +2.5 ‰ (Table 4). The $\delta^{34}S_{CDT}$ of sulfides and $\delta^{18}O_{SMOW}$ of water vary in a narrow range, which suggests a restricted sulfur and oxygen source for the primary mineralization (e.g., Ohmoto, 1986; Ohmoto and Goldhaber, 1997). The herein reported isotopic data, particularly the $\delta^{34}S_{CDT}$, are similar to some orogenic gold deposits in the world such as the New Celebration and Victory deposits in Australia, and Suoluogou in China, supporting the orogenic-type nature of the Namicupo prospect (e.g., Hodkiewicz et al., 2009; Hodge, 2010; Goldfarb and Groves, 2015; Sun et al., 2020; Fig. 12). The mineralized quartz veins in the Namicupo prospect were emplaced along the S1 foliation of metasedimentary rocks of the Xixano Complex, suggesting that the mineralization was contemporaneous to the prograde metamorphism of the rocks of the host terrane. As such, the ore-forming fluid could be formed from the devolatilization of rocks of the Xixano Complex, during prograde metamorphism. The lack of evidence of hydrothermal alteration related with primary mineralization such as sulfidation and carbonation of host rocks suggests that the ore-forming fluid was in equilibrium with the host rocks and the effect of fluid-rock interaction

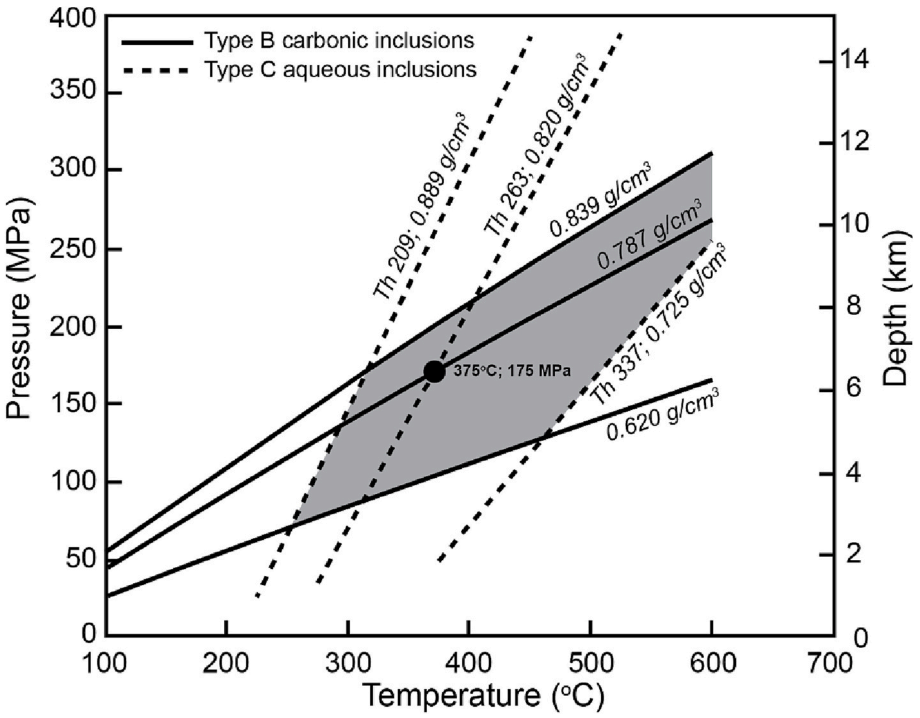

Fig. 11. Pressure and temperature conditions of mineralization based on the intersection of isochores of coexisting Type B CO_2-rich (carbonic) and Type C aqueous inclusions. The isochores of the highest, average, and lowest density Type B and Type A inclusions were plotted. The isochores of average densities intercect at temperature and pressure of 375 °C and 175 MPa, respectively. The corresponding depths were calculated assuming the density of upper lithosphere of 2.7 g/cm^3, under a lithostatic pressure condition.

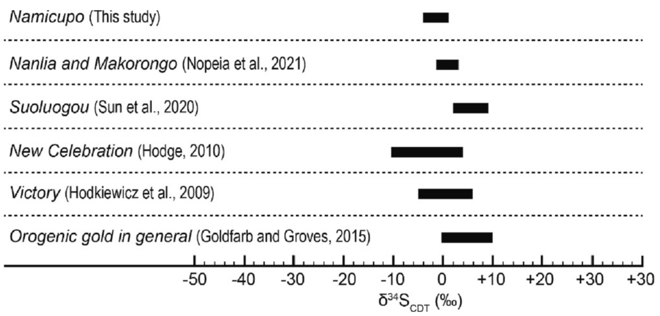

Fig. 12. Comparison of sulfur isotopic ratios of sulfides in primary mineralization for the Namicupo prospect with those of different orogenic-type gold deposits.

was insignificant. The $\delta^{34}S_{CDT}$ and $\delta^{18}O_{SMOW}$ of water could therefore represent the sulfur and oxygen isotopic signatures of the source, which could probably be the rocks of the host terrane, composed of meta-sedimentary rocks and orthogneiss.

5.1.3. Precipitation mechanism of gold

Most researchers agree that gold in orogenic-type gold systems is transported as a sulfide complex (Phillips and Groves, 1983; Benning and Seward, 1996; Schmidt and Seward, 2017). There are several mechanisms that could lead to the breakdown of $Au(HS)_2^-$ complex and consequent precipitation of gold, including: (1) fluid-rock interaction accompanied by sulfidation processes, whereby the H_2S-rich fluid reacts with Fe-bearing minerals from wall rocks and form pyrite, resulting in consumption of H_2S in ore solutions (Phillips and Groves, 1983); (2) a sudden temperature or pressure drop (Sibson et al., 1988; Simmons et al., 2000; Hodkiewicz et al., 2009; Zhang and Zhu, 2017); (3) a combination of both. The first process can be ruled out at Namicupo because no sulfidation was observed in the host rocks in this study. Thus, we consider that the drop of P-T conditions was the main factor that caused the precipitation of gold in the Namicupo prospect, which is supported by the fluid immiscibility revealed by the fluid inclusions. Migration of ore fluids towards the shallower portion and/or fracture openings would have caused the decrease of pressure and temperature of the fluids (e.g., Wilkinson and Johnston, 1996; Sibson et al., 1988).

5.2. The Stage II (supergene) mineralization

The Stage II mineralization in the Namicupo prospect is represented by Ag-rich electrum (with Ag contents varying from 39 to 46 at.%) intergrown with goethite, minium and barite, which replaced partially or totally the primary sulfides. The intergrowth relationship between Ag-rich electrum and goethite and minium suggests that Ag-rich electrum was co-precipitated with these late-formed oxide phases. Thus, the Stage II gold mineralization in the Namicupo prospect is interpreted as supergene gold mineralization.

Supergene gold mineralization generally involves low temperature alteration of primary gold-bearing phases, followed by gold dissolution and reprecipitation, with mobilization on a scale of micrometers to tens of meters distant from the primary source (Stoffregen, 1986; Craw and Kerr, 2017). Gold concentration of pyrite and chalcopyrite associated with primary mineralization reaches 500 ppm in the Namicupo prospect (Fig. 6b). It is likely that gold was liberated from primary Au-rich electrum and gold-bearing minerals through oxidation caused by near surface water (e.g., Craw et al., 2015; Craw and Kerr, 2017). The close spatial distribution of supergene and primary hypogene mineralization suggests that the dissolution of primary minerals and reprecipitation of supergene mineralization at Namicupo took place largely in situ, with little evidence of distant (centimeter to meter) mobilization.

Chemical mobilization of gold by near surface water commonly occurs as a chloride complex in acidic conditions (Webster, 1986; Colin and Viellard, 1991). Since the solubility of silver in chloride-complex is relatively higher than that of gold, the mobilized electrum by chloride-complexes is commonly Ag-poorer than the primary electrum (Webster and Mann, 1984; Webster, 1986; Stoffregen, 1986). However, the supergene electrum in the Namicupo prospect has considerable amounts of silver, up to 46 at.%, higher than the primary electrum. This suggests that a ligand other than chloride was responsible for mobilization of gold and silver in the Namicupo prospect. The coexistence of Ag-rich electrum and barite, and the S contents of supergene Ag-rich electrum, up to 1200 ppm, suggest that gold was remobilized as thiosulfate complex in the Stage II supergene mineralization of the Namicupo prospect. Thiosulfate ion ($S_2O_3^{2-}$) is known to be corrosive to transition metals, especially silver and also gold (Webster, 1986; Craw and Kerr, 2017). It is recognized that thiosulfate can be formed as an intermediate product by the oxidation process of sulfur to sulfate (Bowell, 1991). In the presence of thiosulfate, both silver and gold are transported as thiosulfate complexes so that supergene electrum retains significant silver contents (Webster and Mann, 1984; Stoffregen, 1986; Webster, 1986). We therefore suggest that thiosulfate was the dominant aqueous sulfur species during the supergene process, which was caused by incomplete oxidation of primary Au-rich electrum and gold-bearing sulfides, in the Namicupo prospect. The gold and silver thiosulfate complexes would have occurred in moderately acidic and oxidizing environment, considering that aqueous thiosulfate is unstable in low pH strongly acidic condition, as it is readily disproportionated into elemental sulfur and sulfur dioxide (e.g., Webster, 1986). The precipitation of supergene Ag-rich electrum likely resulted from destabilization of thiosulfate by the change of redox conditions.

The gold mineralization at Namicupo is hosted in the lowest stratigraphic unit of the Xixano Complex. A rapid near-isothermal decompression and subsequent cooling after high-grade metamorphism have been recorded in CDNC rock units (Jamal, 2005; Engvik et al., 2007). The supergene gold enrichment was likely facilitated by uplift and denudation of the Xixano Complex that subjected the primary hypogene ores to weathering at shallower depths.

6. Conclusions

The Namicupo gold prospect is classified as an orogenic-type gold deposit. Gold mineralization in the Namicupo prospect occurred in two stages. The primary mineralization in the Stage I, represented by Au-rich electrum associated with sulfides, was formed by aqueous-carbonic metamorphic fluids. The precipitation of primary electrum was mainly caused by the decrease of pressure and temperature of hydrothermal fluids, which accompanied fluid immiscibility. Supergene mineralization in the Stage II consisted of precipitation of Ag-rich electrum intergrown with goethite, minium, and barite. The supergene gold enrichment was caused by oxidation of primary gold-bearing sulfides and Au-rich electrum under moderately acidic conditions, which resulted in liberation of gold and silver and subsequent chemical mobilization as thiosulfate complexes. The supergene mobilization of primary ores was facilitated by denudation and cooling of the hosting terrane, which subjected primary ores to weathering at shallower depths.

CRediT authorship contribution statement

Manuel Nopeia: conceptualization, data curation and interpretation, writing (the original draft, review and editing). Akira Imai: conceptualization, supervision, data interpretation, writing (review and editing), and funding acquisition. Ryohei Takahashi: supervision, data interpretation, writing (review and editing), and finding acquisition. Kotaro Yonezu: supervision, data interpretation, and funding acquisition. Pearlyn Manalo and Thomas Tindell: supervision, data curation and interpretation, writing (review and editing). Hinako Sato: supervision, data acquisition and validation. Daúd Jamal and Andrea Agangi: supervision, investigation, data interpretation, and writing (review and

editing).

Declaration of competing interest

The authors declare that they have no known competing financial interests or personal relationships that could have appeared to influence the work reported in this paper.

Data availability

Data will be made available on request.

Acknowledgements

We are grateful to Mr. Simão Diquissone for his assistance during the field work, and all members of Economic Geology Laboratories from Kyushu University and Akita University for their insightful comments. This study was financially supported by the Japan International Cooperation Agency (JICA) through KIZUNA Program, the Society of Economic Geologists Foundation with Grant Number SRG_21-41, JSPS KAKENHI Grant Numbers 21K04960 and 21KK0089, and the Japan Mining Promotive Foundation and the Society of Resource Geology. We would like to express our sincere gratitude to two anonymous reviewers for their critical review and valuable comments that significantly improved this manuscript.

References

Agangi, A., Hofmann, A., Przybyłowicz, W., 2014. Trace element zoning of sulfides and quartz at Sheba and Fairview gold mines: Clues to Mesoarchean mineralization in the Barberton Greenstone Belt, South Africa. Ore Geol. Rev. 56, 94–114. https://doi.org/10.1016/j.oregeorev.2013.08.016.

Bakker, R.J., 2003. Package FLUIDS 1. Computer programs for analysis of fluid inclusions data and for modelling bulk fluid properties. Chem. Geol. 194, 2–23. https://doi.org/10.1016/S0009-2541(02)00268-1.

Bakker, R.J., Brown, P.E., 2003. Computer modelling in fluid inclusion research. In: Fluid Inclusions: Analysis and Interpretation, 32. Mineralogical Association of Canada, pp. 175–212.

Benning, L.G., Seward, T.M., 1996. Hydrosulfide complexing of Au (I) in hydrothermal solutions from 150–400 °C and 500–1500 bar. Geochim. Cosmochim. Acta 60, 1849–1871.

Bingen, B., Jacobs, J., Viola, G., Henderson, I.H.C., Skår, Ø., Boyd, R., Thomas, R.J., Solli, A., Key, R.M., Daudi, E.X.F., 2009. Geochronology of the Precambrian crust in the Mozambique belt in NE Mozambique, and implications for Gondwana assembly. Precambrian Res. 170, 231–255. https://doi.org/10.1016/j.precamres.2009.01.005.

Bjerkgard, T., Stein, H.J., Bingen, B., Henderson, I.H.C., Sandstad, J.S., Moniz, A., 2009. The Niassa Gold Belt, northern Mozambique–a segment of a continental-scale Pan-African gold-bearing structure? J. Afr. Earth Sci. 53, 45–58. https://doi.org/10.1016/j.jafrearsci.2008.09.003.

Bodnar, R.J., 1993. Revised equation and table for determining the freezing point depression of H2O-NaCl Solutions. Geochim. Cosmochim. Acta 57, 668–684.

Bowell, R.J., 1991. Supergene gold mineralogy at Ashanti, Ghana: implications for the supergene behavior of gold. Mineral. Mag. 56, 545–560. https://doi.org/10.1180/minmag.1992.056.385.10.

Boyd, R., Nordgulen, Ø., Thomas, R.J., Bingen, B., Bjerkgard, T., Grenne, T., Solli, A., 2010. The geology and geochemistry of the East African Orogen in northeastern Mozambique. S. Afr. J. Geol. 113, 87–129. https://doi.org/10.2113/gssajg.113.1.87.

Bozzo, A.T., Hsiao-Sheng, C., Kass, J.R., Barduhn, A.J., 1975. The properties of the hydrates of chlorine and carbon dioxide. Desalination 16, 303–320. https://doi.org/10.1016/S0011-9164(00)88004-2.

Bralia, A., Sabatini, G., Troja, F., 1979. A revelation of the Co/Ni ratio in pyrite as geochemical tool in ore genesis problems. Mineraium Deposita 14, 353–374.

Chai, P., Hou, Z.Q., Zhang, Z.Y., 2017. Geology, fluid inclusion and stable isotope constraints on the fluid evolution and resource potential of the Xiadian gold deposit, Jiaodong Peninsula. Resour. Geol. 67, 341–359. https://doi.org/10.1111/rge.12134.

Clayton, R.N., Mayeda, T., 1963. The use of bromine pentafluoride in the extraction of oxygen from oxides and silicates for isotopic analysis. Geochim. Cosmochim. Acta 27, 47–52.

Clayton, R.N., O'Neil, J.R., Mayeda, T.K., 1972. Oxygen isotope exchange between quartz and water. J. Geophys. Res. 77, 3057–3067. https://doi.org/10.1029/JB077i017p03057.

Colin, F., Viellard, P., 1991. Behavior of gold in the lateritic equatorial environment: weathering and surface dispersion of residual gold particles, at Dondo Mobi, Gabon. Appl. Geochem. 6, 279–290. https://doi.org/10.1016/0883-2927%2891%2990005-A.

Cossa, E.P., Agangi, A., Takahashi, R., Manalo, P., Imai, A., Manjate, V., 2023. Geology, geochemistry, and genesis of gold mineralization in the Chifumbazi deposit of the Tete Province, Irumide Belt, Mozambique. Resource Geology 73, e12308.

Craw, D., Kerr, G., 2017. Geochemistry and mineralogy of contrasting supergene gold alteration zones, southern Newt Zealand. Appl. Geochem. 85, 19–34. https://doi.org/10.1016/j.apgeochem.2017.08.005.

Craw, D., MacKenzie, D., Grieve, P., 2015. Supergene gold mobility in orogenic gold deposits, Otago Schist, New Zealand. N. Z. J. Geol. Geophys. 58, 123–136.

Duschek, W., Kleinrahm, R., Wagner, W., 1990. Measurement and correlation of the (pressure, density, temperature) relation of carbon dioxide II. Saturated-liquid and saturated-vapour densities and the vapour pressure along the entire coexistence curve. J. Chem. Thermodyn. 22, 841–864.

Engvik, A.K., Tveten, E., Bingen, B., Viola, G., Erambert, M., Feito, P., De Azavedo, S., 2007. PTt evolution and textural evidence for decompression of Pan-African high-pressure granulites, Lurio Belt, North-Eastern Mozambique. J. Metamorph. Geol. 25, 935–952.

Fritz, H., Abdelsalam, M., Ali, K.A., Bingen, B., Collins, A.S., Fowler, A.R., Ghebreab, W., Hauzenberger, C.A., Johnson, P.R., Kusky, T.M., Macey, P., Muhongo, S., Stern, R.J., Viola, G., 2013. Orogen styles in the East African Orogen: a review of the Neoproterozoic to Cambrian tectonic evolution. J. Afr. Earth Sci. 86, 65–106. https://doi.org/10.1016/j.jafrearsci.2013.06.004.

Goldfarb, R.J., Groves, D.I., 2015. Orogenic gold: Common or evolving fluid and metal sources through time. Lithos 233, 2–26. https://doi.org/10.1016/j.lithos.2015.07.011.

Goldfarb, R.J., Baker, T., Dube, B., Groves, D.I., Hart, C.J., Gosselin, P., 2005. Distribution, character and genesis of gold deposits in metamorphic terranes. In: Society of Economic Geologists 100th Anniversary Volume, pp. 407–450.

Grantham, G.H., Macey, P.H., Horie, K., Kawakami, T., Ishikawa, M., Satish-Kumar, M., Tsuchiya, N., Graser, P., Azevedo, S., 2013. Comparison of the metamorphic history of the Monapo Complex, northern Mozambique and Balchenfjella and Austhameren areas, Sør Rondane, Antarctica: implications for the Kuunga Orogeny and the amalgamation of N and S. Gondwana. Precambrian Research 234, 85–135. https://doi.org/10.1016/j.precamres.2012.11.012.

Hilson, G., Mondlane, S., Hilson, A., Arnall, A., Laing, T., 2021. Formalizing artisanal and small-scale mining in Mozambique: concerns, priorities and challenges. Resources Policy 71, 102001. https://doi.org/10.1016/j.resourpol.2021.102001.

Hodge, J.L., 2010. Hydrothermal Evolution of Two Stage of Gold Mineralization at the Orogenic New Celebration Gold Deposit, and Implications for Gold Mineralization Within the Kalgoorlie-Kambalde Corridor, Eastern Goldfields Province, Western Australia. Dissertation for Doctoral Degree. University of Western Australia, 393 p.

Hodkiewicz, P.F., Groves, D.I., Davidson, G.J., Weinberg, R.F., Hagemann, S.G., 2009. Influence of structural setting on Sulphur isotopes in Archean orogenic gold deposits, Eastern Goldfields Province, Yilgarn, Western Australia. Mineral. Deposita 44, 129–150. https://doi.org/10.1007/s00126-008-0211-5.

Itano, K., Iizuka, T., Chang, Q., Kimura, J.I., Maruyama, S., 2016. U-Pb chronology and geochemistry of detrital monazites from major african rivers: Constraints on the timing and nature of the Pan-African Orogeny. Precambrian Res. 282, 139–156. https://doi.org/10.1016/j.precamres.2016.07.008.

Jamal, D.L., 2005. Crustal Studies Across Selected Geotransects in NE Mozambique: Differentiating Between Mozambiquan (Kibaran) and Pan-African Events, With Implications for Gondwana Studies. University of Cape Town.

Khomyakov, A.P., 1983. Natrite, Na2CO3–a new mineral. Int. Geol. Rev. 25, 1111–1116.

Korkiakoski, E., 2008. Geochemical surveys in Mozambique: a data compilation project. Geol. Surv. Finland Spec. Pap. 48, 263–287.

Lächelt, S., 2004. Geological and Mineral Resources of Mozambique. Ministério de Recursos Minerais e Energia de Moçambique, 515 p.

Li, H., Wu, Q.H., Evans, N.J., Zhou, Z.K., Kong, H., Xi, X.S., Lin, Z.W., 2018. Geochemistry and geochronology of the Banxi Sb deposit: Implications for fluid origin and the evolution of Sb mineralization in Central-Western Hunan, South China. Gondwana Res. 55, 112–134. https://doi.org/10.1016/j.gr.2017.11.010.

Macey, P.H., Miller, J.A., Rowe, C.D., Grantham, G.H., Siegfried, P., Armstrong, R.A., Bacalau, J., 2013. Geology of the Monapo Klippe, NE Mozambique and its significance for assembly of Central Gondwana. Precambrian Res. 233, 259–281. https://doi.org/10.1016/j.precamres.2013.03.012.

Malta, I.S., Faleiros, F.M., Monteiro, L.V., Andrade, M.B., Coldebella, B., Esteves, M.C., 2020. PT-fluid-deformation regime of the Ediacaran Serra do Cavalo Magro orogenic gold deposit, Ribeira Belt, Brazil. Ore Geol. Rev. 120, 1–26. https://doi.org/10.1016/j.oregeorev.2020.103384.

Manalo, P.C., Imai, A., Subang, L.L., de los Santos, M., Yanagi, K., Takahashi, R., Blamey, N.J.F., 2018. Mineralization of the Northwest quartz-pyrite-gold veins: implications for multiple mineralization events at Lepanto, Mankayan Mineral District, northern Luzon, Philippines. Economic Geology 113, 1609–1626.

McInnes, M., Greenough, J.D., Fryer, B.J., Wells, R., 2008. Trace elements in native gold by solution ICP-MS and their use in mineral exploration: a British Columbia example. Appl. Geochem. 23, 1076–1085. https://doi.org/10.1016/j.apgeochem.2007.12.027.

Meert, J.G., 2003. A synopsis of events related to the assembly of eastern Gondwana. Tectonophysics 362, 1–40. https://doi.org/10.1016/S0040-1951(02)00629-7.

Melezhik, V.A., Bingen, B., Fallick, A.E., Gorokhov, I.M., Kuznetsov, A.B., Sandstad, J.S., Jamal, D., 2008. Isotope chemostratigraphy of marbles in northeastern Mozambique: apparent depositional ages and tectonostratigraphic implications. Precambrian Res. 162, 540–558. https://doi.org/10.1016/j.precamres.2007.11.002.

Mishra, B., Panigrahi, M.K., 1999. Fluid evolution in the Kolar Gold Field: evidence from fluid inclusion studies. Mineral. Deposita 34, 173–181.

Nopeia, M., Takahashi, R., Imai, A., Jamal, D., Agangi, A., 2021. Geological and geochemical characterization of the Nanlia and Makorongo gold prospects, Mozambique Belt, northeastern Mozambique. Ore Geol. Rev. 135, 104195 https://doi.org/10.1016/j.oregeorev.2021.104195.

Nopeia, M., Mondlane, S., Takahashi, R., Jamal, D., Abdulgani, I., Baptista, I., 2022. An integrated geoscience approach to effective formalization of artisanal mining in Mozambique: a case study of Namuno District, northeastern Mozambique. In: The Extractive Industries and Society, 101098. https://doi.org/10.1016/j.exis.2022.101098.

Norconsult Consortium, 2007. Mineral Resources Management Capacity Building Project, Republic of Mozambique; Component 2: Geological Infrastructure Development Project; Geological Mapping, Lot 1; Sheet explanation: 32 Sheets; Scale: 1/250 000, Report No. B6. National Directorate of Geology, Republic of Mozambique, 778 p.

Ohmoto, H., 1986. Stable isotope geochemistry of ore deposits. In: Valley, J.W., Taylor, H.P., O'Neil, J.R. (Eds.), Stable Isotopes in High Temperature Geological Processes. Reviews in Mineralogy, 16, pp. 491–560.

Ohmoto, H., Goldhaber, M.B., 1997. Sulfur and carbon isotopes. In: Barnes, H.L. (Ed.), Geochemistry of Hydrothermal Deposits, 3rd ed. Wiley, New York, pp. 517–611.

Phillips, G.N., Groves, D.I., 1983. The nature of Archaean gold-bearing fluids as deduced from gold deposits of Western Australia. J. Geol. Soc. Aust. 30, 25–39. https://doi.org/10.1080/00167618308729234.

Phillips, G.N., Powell, R., 2010. Formation of gold deposits: a metamorphic devolatilization model. J. Metamorph. Geol. 28, 689–718. https://doi.org/10.1111/j.1525-1314.2010.00887.x.

Pinna, P., Jourde, G., Calvez, J.Y., Mroz, J.P., Marques, J.M., 1993. The Mozambique Belt in northern Mozambique: Neoproterozoic (1100–850 Ma) crustal growth and tectogenesis, and superimposed Pan-African (800–550 Ma) tectonism. Precambrian Res. 62, 1–59. https://doi.org/10.1016/0301-9268(93)90093-H.

Ramboz, C., Pichavant, M., Weisbrod, A., 1982. Fluid immiscibility in natural processes: use and misuse of fluid inclusion data: II. Interpretation of fluid inclusion data in terms of immiscibility. Chem. Geol. 37, 29–48. https://doi.org/10.1016/0009-2541(82)90065-1.

Reich, M., Kesler, S.E., Utsunomiya, S., Palenik, C.S., Chryssoulis, S.L., Ewing, R.C., 2005. Solubility of gold in arsenian pyrite. Geochim. Cosmochim. Acta 69, 2781–2796. https://doi.org/10.1016/j.gca.2005.01.011.

Reich, M., Simon, A.C., Deditius, A., Barra, F., Chryssoulis, S., Lagas, G., Tardani, D., Knipping, J., Bilenker, L., Sánchez-Alfaro, P., Roberts, M.P., Munizaga, R., 2016. Trace element signature of pyrite from the Los Colorados iron oxide-apatite (IOA) deposit, Chile: a missing link between Andean IOA and iron oxide copper-gold systems? Econ. Geol. 3, 743–761. https://doi.org/10.2113/econgeo.111.3.743.

Ridley, J.R., Diamond, L.W., 2000. Fluid chemistry of lode-gold deposits and implications for genetic models. In: Hagemann, S.G., Brown, P. (Eds.), Gold in 2000. Reviews in Economic Geology, Society of Economic Geologists, 13, pp. 141–162.

Roedder, E., 1984. Fluid inclusions. In: Reviews in Mineralogy, Mineralogical Society ofAmerica, 12, 646 p.

Roedder, E., Bodnar, R.J., 1980. Geologic pressure determinations from fluid inclusion studies. Annu. Rev. Earth Planet. Sci. 8, 263–301. https://doi.org/10.1146/annurev.ea.08.050180.001403.

Schmidt Mumm, A.H., Oberthür, T., Vetter, U., Blenkinsop, T.G., 1997. High CO2 content of fluid inclusions in gold mineralization in the Ashanti Belt, Ghana: a new category of ore forming fluids? Mineral. Deposita 32, 107–118.

Schmidt, C., Seward, T.M., 2017. Raman spectroscopic quantification of sulfur species in aqueous fluids: Ratios of relative molar scattering factors of Raman bands of H2S, HS-, SO2, HSO4−, SO42−, S2O32−, S3− and H2O at ambient conditions and information on changes with pressure and temperature. Chem. Geol. 467, 64–75. https://doi.org/10.1016/j.chemgeo.2017.07.022.

Sibson, R.H., Robert, F., Poulsen, K.H., 1988. High-angle reverse faults, fluid-pressure cycling, and mesothermal gold-quartz deposits. Geology 16, 551–555. https://doi.org/10.1130/0091-7613(1988)016%3C0551:HARFFP%3E2.3.CO;2.

Simmons, S.F., Arehart, G., Simpson, M.P., Mauk, J.L., 2000. Origin of massive calcite veins in the Golden Cross low-sulfidation, epithermal Au-Ag deposit, New Zealand. Econ. Geol. 95, 99–112. https://doi.org/10.2113/gsecongeo.95.1.99.

Span, R., Wagner, W., 1996. A new equation of state for carbon dioxide covering the fluid region from the triple-point temperature to 1100 K at pressures up to 800 MPa. J. Phys. Chem. Ref. Data 25, 1509–1596. https://doi.org/10.1063/1.555991.

Spear, F.S., 1993. Metamorphic phase equilibria and pressure-temperature-time paths. In: Mineralogical Society of America, Monograph, Michigan, USA.

Stoffregen, R., 1986. Observations on the behavior of gold during supergene oxidation at Summitville, Colorado, USA, and implications for electrum stability in the weathering environment. Appl. Geochem. 1, 549–558. https://doi.org/10.1016/0883-2927(86)90062-4.

Sun, P., Wang, Q., Li, H., Dong, C., Deng, J., 2020. Geology and pyrite sulfur isotopes of the Suoluogou gold deposit: Implication for crustal continuum model of orogenic gold deposit in northwestern margin of Yangtze CratonSW China. Ore Geology Reviews 122, 103487. https://doi.org/10.1016/j.oregeorev.2020.103487.

Viola, G., Henderson, I.H.C., Bingen, B., Thomas, R.J., Smethurst, M.D., De Azavedo, S., 2008. Growth and collapse of a deeply eroded orogen: insights from structural, geophysical, and geochronological constraints on the Pan-African evolution of NE Mozambique. Tectonics 27, 1–31. https://doi.org/10.1029/2008TC002284.

Webster, J.G., 1986. The solubility of gold and silver in the system Au-Ag-S-O2-H2O at 25° C and 1 atm. Geochim. Cosmochim. Acta 50, 1837–1845.

Webster, J.G., Mann, A.W., 1984. The influence of climate, geomorphology and primary geology on the supergene migration of gold and silver. J. Geochem. Explor. 22, 21–42. https://doi.org/10.1016/0375-6742(84)90004-9.

Wilkinson, J.J., 2001. Fluid inclusions in hydrothermal ore deposits. Lithos 55, 229–272. https://doi.org/10.1016/S0024-4937(00)00047-5.

Wilkinson, J.J., Johnston, J.D., 1996. Pressure fluctuations, phase separation, and gold precipitation during seismic fracture propagation. Geology 24, 395–398. https://doi.org/10.1130/0091-7613(1996)024<0395:PFPSAG>2.3.CO;2.

Yanagisawa, F., Sakai, H., 1983. Thermal decomposition of barium sulfate-vanadium pentoxide-silica glass mixtures for preparation of sulfur dioxide in sulfur isotope ratio measurements. Anal. Chem. 55, 985–987.

Zhang, Y.G., Frantz, J.D., 1987. Determination of homogenization temperatures and densities of supercritical fluids in the system NaCl-KCl-CaCl2-H2O using synthetic fluid inclusions. Chem. Geol. 64, 335–350.

Zhang, H., Zhu, Y., 2017. Genesis of the Mandongshan gold deposit (Xinjiang, NW China): T-P-fS2 and phase equilibria constraints from the Au-As-Fe-S system. Ore Geol. Rev. 83, 135–151. https://doi.org/10.1016/j.oregeorev.2016.11.032.